PRACTICAL SPECTROSCOPY SERIES VOLUME 30

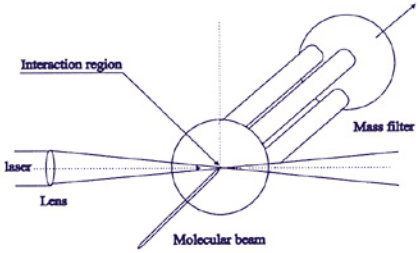

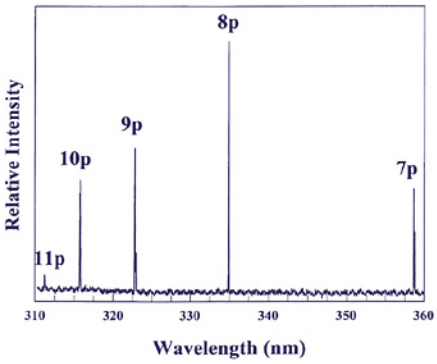

Ultraviolet Spectroscopy and UV Lasers

edited by
Prabhakar Misra
Mark A. Dubinskii

Also available as a printed book
see title verso for ISBN details

Ultraviolet Spectroscopy and UV Lasers

PRACTICAL SPECTROSCOPY

A SERIES

1. Infrared and Raman Spectroscopy (in three parts), *edited by Edward G. Brame, Jr, and Jeanette G.Grasselli*

2. X-Ray Spectrometry, *edited by H.K.Herglotz and L S.Birks*

3. Mass Spectrometry (in two parts), *edited by Charles Merritt, Jr., and Charles N.McEwen*

4. Infrared and Raman Spectroscopy of Polymers, *H.W.Siesler and K. Holland-Moritz*

5. NMR Spectroscopy Techniques, *edited by Cecil Dybowski and Robert L. Lichter*

6. Infrared Microspectroscopy: Theory and Applications, *edited by Robert G. Messerschmidt and Matthew A.Harthcock*

7. Flow Injection Atomic Spectroscopy, *edited by Jose Luis Burguera*

8. Mass Spectrometry of Biological Materials, *edited by Charles N.McEwen and Barbara S.Larsen*

9. Field Desorption Mass Spectrometry, *László Prókai*

10. Chromatography/Fourier Transform Infrared Spectroscopy and Its Applications, *Robert White*

11. Modern NMR Techniques and Their Application in Chemistry, *edited by Alexander I.Popov and Klaas Hallenga*

12. Luminescence Techniques in Chemical and Biochemical Analysis, *edited by Willy R.G.Baeyens, Denis De Keukeleire, and Katherine Korkidis*

13. Handbook of Near-Infrared Analysis, *edited by Donald A.Burns and Emil W. Ciurczak*

14. Handbook of X-Ray Spectrometry: Methods and Techniques, *edited by René E.Van Grieken and Andrzej A.Markowicz*

15. Internal Reflection Spectroscopy: Theory and Applications, *edited by Francis M.Mirabella, Jr.*

16. Microscopic and Spectroscopic Imaging of the Chemical State, *edited by Michael D.Morris*

17. Mathematical Analysis of Spectral Orthogonality, *John H.Kalivas and Patrick M.Lang*

18. Laser Spectroscopy: Techniques and Applications, *E.Roland Menzel*

19. Practical Guide to Infrared Microspectroscopy, *edited by Howard J.Humecki*

20. Quantitative X-ray Spectrometry: Second Edition, *Ron Jenkins, R.W.Gould, and Dale Gedcke*

21. NMR Spectroscopy Techniques: Second Edition, Revised and Expanded, *edited by Martha D.Bruch*

22. Spectrophotometric Reactions, *Irena Nemcova, Ludmila Cermakova, and Jiri Gasparic*

23. Inorganic Mass Spectrometry: Fundamentals and Applications, *edited by Christopher M.Barshick, Douglas C.Duckworth, and David H.Smith*

24. Infrared and Raman Spectroscopy of Biological Materials, *edited by Hans-Ulrich Gremlich and Bing Yan*

25. Near-Infrared Applications in Biotechnology, *edited by Ramesh Raghavachari*

26. Ultrafast Infrared and Raman Spectroscopy, *edited by M.D.Fayer*

27. Handbook of Near-Infrared Analysis: Second Edition, Revised and Expanded, *edited by Donald A.Burns and Emil W.Ciurczak*

28. Handbook of Raman Spectroscopy: From the Research Laboratory to the Process Line, *edited by Ian R.Lewis and Howell G.M.Edwards*

29. Handbook of X-Ray Spectrometry: Second Edition, Revised and Expanded, edited by *René E.Van Grieken and Andrzej A.Markowicz*

30. Ultraviolet Spectroscopy and UV Lasers, *edited by Prabhakar Misra and Mark A.Dubinskii*

31. Pharmaceutical and Medicinal Applications of Near-Infrared Spectroscopy, *Emil W.Ciurczak and James K.Drennen III*

ADDITIONAL VOLUMES IN PREPARATION

Applied Electrospray Mass Spectrometery, *edited by Birendra N.Pramanik, A.K.Ganguly, and Michael L.Gross*

Ultraviolet Spectroscopy and UV Lasers

edited by

Prabhakar Misra
Howard University
Washington, D.C.

Mark A.Dubinskii
Magnon, Inc.
Reisterstown, Maryland

MARCEL DEKKER, INC. NEW YORK • BASEL

This edition published in the Taylor & Francis e-Library, 2005.

ISBN 0-203-90832-5 Master e-book ISBN

ISBN: 0-8247-0668-4 (Print Edition)

Headquarters
Marcel Dekker, Inc.
270 Madison Avenue, New York, NY 10016
tel: 212–696–9000; fax: 212–685–4540

Eastern Hemisphere Distribution
Marcel Dekker AG
Hutgasse 4, Postfach 812, CH-4001 Basel, Switzerland
tel: 41–61–261–8482; fax: 41–61–261–8896

World Wide Web
http://www.dekker.com

The publisher offers discounts on this book when ordered in bulk quantities. For more information, write to Special Sales/Professional Marketing at the headquarters address above.

Preface

Ultraviolet Spectroscopy and UV Lasers covers a range of subjects, from ultraviolet (UV) and vacuum ultraviolet (VUV) sources to the latest advances in instrumentation and techniques for absorption, emission, and fluorescence spectroscopy. The book will prove useful to scientists pursuing spectroscopy-related research in fields as varied and diverse as optical physics and engineering, analytical chemistry, biology, and laser technology. The book can also serve as a reference text for a two-semester special topics course for upper-level undergraduate and graduate students in these disciplines.

In the opening chapter, "Ultraviolet and Vacuum Ultraviolet Sources and Materials for Lithography," Liberman and Rothschild review radiation sources in the UV and VUV, followed by an appraisal of the key factors governing efficient detection of UV radiation. Their overview of sources and detectors, although presented in the context of lithographic applications, will prove useful for other UV spectroscopic applications as well. UV optical metrology is covered under two subheadings: measurements of bulk material properties and surfaces and measurement of thin film properties. Candidate optical materials for lithographic systems are reviewed in light of their index homogeneity, birefringent properties, and durability. An important consideration in the use of optical components for metrological applications at UV wavelengths is the issue of large absorption coefficients exhibited by vapors and surface adsorbates, which is the subject of discussion in the concluding segment of this chapter.

The second chapter, "Laser Optogalvanic Spectroscopy of Discharge Plasmas in the Ultraviolet Region" is coauthored by one of the editors (PM) of this book and provides an overview of the optogalvanic effect. Owing to its sensitivity and selectivity, the optogalvanic technique has been utilized for a wide variety of spectroscopic applications, including analytical flame spectrometry, atomic and molecular spectroscopy, laser stabilization and calibration, and plasma diagnostics. Haridass, Major, Misra, and Han provide both an experimental background and a theoretical framework for reporting an extensive array of optogalvanic spectral transitions and selective waveforms in the UV for both neon and argon. The mechanism associated with the generation of the optogalvanic signal is covered in depth, and a theoretical model is developed and used to analyze and interpret time-resolved waveforms of specific optogalvanic transitions of neon and argon in the context of electron collisional ionization and electron collisional transfer rates in a discharge medium.

In Chapter 3, "Spectra of the Isotopomers of CO^+, N_2^+, and NO in the Ultraviolet," Reddy and Haridass describe the experimental recording of data with a hollow cathode discharge tube, followed by a subsequent detailed analysis of the electronic spectra of these species. The ultraviolet spectroscopy of these molecules is important for the understanding and elucidation of significant astrophysical processes, as well as for improved understanding of associated terrestrial environmental and combustion phenomena. A review of the relevant electronic configurations and the general

spectroscopic equations needed for a detailed spectral analysis and interpretation is provided. A comprehensive historical overview of past and present work is provided, in turn, for CO^+, N_2^+, and NO, followed by presentation and analysis of UV spectra for the isotopomers of all three molecular species. Schematic energy level diagrams illustrate the allowed spectral transitions and the associated branches in detail. Precise molecular parameters characterizing the various electronic states of the different species have been determined using rigorous nonlinear least-squares fitting routines and are tabulated for easy reference.

Photoabsorption cross-section measurements in the ultraviolet and vacuum ultraviolet are the subject of Chapter 4. Yoshino outlines the earlier cross-section measurements—prior to 1980—and discusses the current instrumentation available for precise cross-section measurements in the UV and VUV. A major uncertainty in cross-section measurements with a single path spectrometer is in estimating the background intensity level, since it may vary with wavelength and time during the course of the photoabsorption scan. It is also often difficult to maintain the gas pressure constant within the absorption cell, particularly for reactive and/ or absorbent species. Yoshino summarizes these difficulties in the context of cross-section measurements of the photoabsorption continuum under lower resolution, citing the specific example of the H_2O molecule. He then reviews measurements of cross-sections for molecular bands possessing associated fine rotational structure under superior resolution in relation to the Doppler widths of relatively simpler molecules. Line-by-line cross-section measurements of the Schumann-Runge bands of O_2 and their temperature dependence are then discussed. Line and band oscillator strengths are subsequently related via the Hönl-London factor, whereby once the band oscillator strengths are established, cross-sections for any temperature can in principle be determined.

In Chapter 5, "Ultraviolet and Vacuum Ultraviolet Laser Spectroscopy Using Fluorescence and Time-of-Flight Mass Detection," Lipson and Shi review the principles and techniques of ultraviolet lasers produced by frequency doubling in anisotropic crystals, nonresonant third harmonic generation, and two-photon resonant four-wave sum- and difference-frequency generation in isotropic gases. Their application focus is on single-photon excitations of supersonically jet-cooled gas-phase molecules that are detected either via laser-induced fluorescence or by ion detection via time-of-flight mass spectrometry. The authors provide a detailed discussion of supersonic jet expansions, which have now been established as a powerful tool for gas-phase spectroscopy, because a jet environment is highly conducive to the production and probing of rovibrationally cold molecules, free radicals, and clusters. This chapter provides practical examples of UV and VUV laser-induced fluorescence and time-of-flight excitation spectra in supersonic jets. The spectroscopy of several metal monohalide radicals and diatomic halogens is presented in some detail. A comprehensive catalog of atomic and molecular systems studied with VUV lasers is provided in tabular form. The table includes a summary of the electronic states investigated by specific spectroscopic methods for various atomic and molecular species, along with the pertinent literature references. The use of VUV lasers in tandem with mass spectrometry provides unique opportunities for detection and characterization of organic molecules. The practical use of these techniques is illustrated in the context of organic molecules (with several examples), and a detailed

referenced tabulation of organic molecular systems detected by nonresonant VUV ionization has been included. The authors also provide a comprehensive bibliography of the literature associated with the twin techniques of fluorescence spectroscopy and time-of-flight mass detection.

In Chapter 6, Cefalas and Sarantopoulou review spectroscopy and applications of diatomic and triatomic molecules assisted by laser light at 157.6 nm. The authors begin with a description of the useful characteristics of the 157.6 nm radiation source—a molecular fluorine laser—and of its utility for photolithography, and then lead up to a summary of the laser's usage for elucidating the spectroscopy of such varied molecules as OH, O_2, HCl, DCl, CH_3Cl, H_2, OCS, H_2O, HDO, ICN, AsF_2, O_3, CO_2, and SiH. Spectroscopic investigations relating to the properties of neutral or charged clusters can be accomplished in the VUV via optical and mass spectroscopic techniques. Such approaches to study clusters in the VUV possess two distinct advantages, namely, that systems with a large band gap can be studied and that excitation of inner shell electrons allows element-specific information to be collected. In this context, the VUV spectroscopy of triatomic clusters is reviewed. It is followed by a discussion of the laser-induced fluorescence and mass spectroscopy of diatomic and triatomic clusters of mercury and a description of the interesting quantum beat phenomenon in mercury triatomic clusters, following de-excitation from the excited state to the ground state.

In "Tunable Solid-State Ultraviolet and Vacuum Ultraviolet Lasers" (Chapter 7), Ilev and Waynant comprehensively review the all-solid-state concept for producing widely tunable short-wavelength laser generation using nonlinear optical techniques and specific solid-state active materials (e.g., the rare-earth-doped wide band gap crystals). The authors provide an analytical outline of the general principles concerning basic nonlinear effects and then consider the primary all-solid-state nonlinear techniques and optical materials utilized for generating tunable UV/VUV radiation. Significant progress achieved by nonlinear frequency upconversion techniques is also presented. Optical fibers provide a good solid-state medium for broad-band optical frequency conversions, and when laser radiation is propagated in such fibers suitable conditions are realized for efficient nonlinear processes, which include, among others, stimulated Raman scattering, four-photon mixing, and self-phase modulation. Nonlinear effects in optical fibers are presented in considerable detail, especially those involving stimulated Raman scattering and its application for the design and development of tunable fiber Raman lasers in the UV. In addition to the all-solid-state nonlinear techniques for tunable UV/VUV laser generation, the use of rare-earth-activated wide band gap fluoride dielectric crystals for the development of solid-state UV/VUV lasers is reviewed, and leads naturally to the subject matter of the next chapter.

In Chapter 8, "VUV Laser Spectroscopy of Trivalent Rare-Earth Ions in Wide Band Gap Fluoride Crystals," methods and techniques used in vacuum ultraviolet spectroscopy are reviewed by Sarantopoulou and Cefalas, with special focus on the molecular fluorine laser and VUV absorption spectroscopy. Optical and electronic properties of wide band gap fluoride dielectric crystals doped with trivalent rare-earth ions are surveyed, followed by a section on the VUV absorption spectroscopy of these ions. Tables provide the energy positions of the $4f^{n-1}5d$ electronic configuration level onsets of the trivalent rare-earth ions in various crystal hosts, together with crystal field splitting of the main $4f^n$

electronic configuration levels in the presence of octahedral and tetragonal symmetry crystal fields. The laser-induced fluorescence spectroscopy of various rare-earth-activating ions excited at 157.6 nm is presented and discussed in relation to the active center formation with different site symmetries, direct emission and/or weak electron-phonon interactions, emission due to repopulation via phonon trapping and reabsorption of lattice vibrations, and spin-forbidden transitions.

In Chapter 9, "Spectroscopy of Broad-Band UV-Emitting Materials Based on Trivalent Rare-Earth Ions" by Moncorgé, the latest developments in broadband UV laser systems are discussed and the pros and cons of using specific rare-earth ions for different applications are evaluated. Data summarizing the positions and fluorescence lifetimes of metastable levels in different hosts doped with rare-earth ions are presented, along with the related excited-state absorption spectra. Color center formation, also known as solarization, following excitation by the UV light, can be a critical problem in UV-emitting materials with direct excitation. Such solarization effects are discussed with respect to polarization of the optical transitions and in relation to the purity and dopant substitution processes associated with the host crystals used.

Oldenburg and Eden, in "Generation of Coherent Ultraviolet and Vacuum Ultraviolet Radiation by Nonlinear Processes in Intense Optical Fields" (Chapter 10) focus on three important processes: continuum generation, four-wave mixing, and high-order harmonic generation. Researchers in the past decade and a half have observed a variety of nonlinear effects that are a direct result of intense optical fields available to them. The generation of odd harmonics when an intense optical field interacts with an atom or molecule in the gas phase offers the potential for the development of a table-top source emitting soft X-ray radiation or coherent XUV. In addition, harmonic generation is also an exceptional tool for investigating the interaction between an atomic system and a strong optical field. The authors explore all of the above issues and their ramifications.

In Chapter 11, Liu, Sarukura, and Dubinskii (a coeditor of this volume) comprehensively review the all-solid-state, short-pulse, tunable, ultraviolet laser sources based on Ce^{3+}-activated fluoride crystals. Rare earth ions incorporated in appropriate host crystals exhibit vibronic lasing and can be implemented for the development of compact and widely tunable ultrashort-pulse laser sources in the UV. Prior to detailed discussions of newer solid-state laser materials, the authors review the existing UV laser systems that use efficient frequency conversion and also those that allow direct generation of coherent UV radiation. The spectroscopic and laser properties of Ce:LLF and Ce:LiCAF crystals are reviewed in depth, followed by a discussion on the generation of subnanosecond pulses from Ce^{3+}-doped fluoride lasers. Short-cavity subnanosecond pulse generation, combined with regenerative amplification, has been used in the design of the novel so-called self-injection-seeded pulse train lasers. The authors introduce a generalized passive version of this device, followed by detailed descriptions of the self-injection-seeded pulse train Ce:LLF and Ce:LiCAF lasers. Tunability data for the short-cavity Ce:LLF and Ce:LiCAF lasers are presented in the near-UV, followed by a demonstration of tunable subnanosecond pulse generation around 230 nm by sum-frequency generation.

Fluorescence lifetime spectroscopy requires UV pulses with pulse durations shorter than the fluorescence lifetime of a large number of molecules. "Diode-Pumped Picosecond UV Lasers by Nonlinear Frequency Conversions" (Chapter 12) addresses the

critical issues related to the development of compact, efficient, and reliable diode-pumped short-pulsed solid-state lasers that can be effectively utilized for such fluorescence lifetime measurements. Balembois et al. present several diode-pumped sources that emit picosecond pulses in the UV. Three kinds of techniques have been used to generate the picosecond pulses (followed by appropriate multipass or regenerative amplification): active mode locking of a laser cavity, gain-switching of a laser diode, and passive Q-switching of an ultra-short-cavity microchip laser. All the sources developed use diode-pumped laser crystals that emit in the near infrared, and the emission is subsequently converted to UV wavelengths utilizing nonlinear crystals for harmonic generation. A pair of laser sources has been developed, based on a Ti: sapphire regenerative amplifier seeded by either an actively mode-locked diode-pumped Cr^{3+}:$LiSrAlF_6$ pico-second oscillator or a gain-switched picosecond laser diode. These lasers produced an average power of 1 mW in the wavelength region 270–285 nm. Another efficient laser source described here is based on a passive Q-switched Nd:YAG laser that seeds a multipass (specifically 2 or 4) Nd:YVO_4 amplifier. Such potentially portable systems hold promise for optical sampling and for the semiconductor industry, besides their obvious utility for fluorescence spectroscopy.

Ultraviolet spectroscopy can provide a wealth of information about the Earth's atmosphere via remote sensing techniques. In "Atmospheric Ultraviolet Spectroscopy," Chance and Rothman survey the field of UV remote sensing measurements, with a special focus on satellite-based measurements. They provide an overview of the underlying physics, followed by a description of the data analysis techniques used to process raw data and extract meaningful atmospheric parameters. The HITRAN spectroscopic database has become the standard reference for absorption cross-section information related to atmospheric measurements. The authors report on the progress and status of the extension of the HITRAN database into the ultraviolet regime, and point out that the UV data are stored in a separate directory in the HITRAN compilation and further subdivided into cross-sectional and line parameter data. The concluding segment of Chapter 13 presents an overview of satellite UV spectrometers that have been used for atmospheric investigations followed by a survey of current and planned instrumentation for atmospheric ultraviolet spectroscopy.

In the final chapter of the book, "Ultraviolet Spectroscopy in Astronomy," Carruthers provides an account of the early measurements and the difficulties encountered in recording UV spectra of astronomical objects. He then describes the characteristics required of materials for transmission optics and those of coatings for reflective optics used in designing efficient UV spectroscopic instrumentation. Typical spectrograph configurations and designs are reviewed in the context of space measurements and stellar observations. The evolution of ultraviolet detectors is reviewed, covering photographic films, photomultipliers, channel electron multipliers, and electronic imaging devices. Examples of current UV spectrographic instruments and their applications to UV space astronomy are presented, which include measurements with the Hubble Space Telescope, the Hopkins UV Telescope, the Interstellar Medium-Absorption Profile Spectrome-ter, and the Far-Ultraviolet Spectroscopic Explorer, as well as Extreme-UV (below about 90 nm) Spectroscopy Missions. A summary of the scientific results from various UV space astronomy missions is provided. Different types of measurements are summarized: those

related to the solar atmosphere and solar activity, those involving temperatures and luminosities of hot stars, as well as measurements of the composition and properties of the interstellar medium and studies relating to extragalactic objects and cosmology.

The editors wish to acknowledge all of the contributors in putting the book together, despite their busy schedules. We would also like to acknowledge Ms. Barbara Mathieu's tireless efforts in this endeavor and appreciate Mr. Russell Dekker's patience and support.

Professor Misra wishes to dedicate this book in fond and cherished memory of his father, Shri Prem Krishna Misra, who always valued a good book. Dr. Dubinskii would like to dedicate his efforts on this book with gratefulness to the memory of his teacher, Professor S.A.Altshuller, one of the true pioneers of electronic paramagnetic resonance and nuclear magnetic resonance.

Prabhakar Misra
Mark A.Dubinskii

Contents

Contributors

F**rançois Balembois, Ph.D.** Non Linear Optics Group, Laboratoire Charles Fabry de l'Institut d'Optique, Orsay, France

A**lain Brun, Ph.D.** Non Linear Optics Group, Laboratoire Charles Fabry de l'Institut d'Optique, Orsay, France

G**eorge R.Carruthers, Ph.D.** Space Science Division, Naval Research Laboratory, Washington, D.C.

A**lciviadis-Constantinos Cefalas, Ph.D.** National Hellenic Research Foundation, Theoretical and Physical Chemistry Institute, Athens, Greece

K**elly Chance, Ph.D.** Atomic and Molecular Physics Division, Harvard-Smithsonian Center for Astrophysics, Cambridge, Massachusetts

F**rédéric Druon, Ph.D.** Non Linear Optics Group, Laboratoire Charles Fabry de l'Institut d'Optique, Orsay, France

M**ark A.Dubinskii, Ph.D.** Magnon, Inc., Reisterstown, Maryland

J**.G.Eden, Ph.D.** Department of Electrical and Computer Engineering, and Office of Vice-Chancellor for Research, University of Illinois, Urbana, Illinois

P**atrick Georges, Ph.D.** Non Linear Optics Group, Laboratoire Charles Fabry de l'Institut d'Optique, Orsay, France

X**ianming L.Han, Ph.D.** Department of Physics and Astronomy, Butler University, Indianapolis, Indiana

C**.Haridass, Ph.D.*** Department of Physics and Astronomy, Howard University, Washington, D.C.

I**lko K.Ilev, Ph.D.** U.S. Food and Drug Administration, Rockville, Maryland

V**ladimir Liberman, Ph.D.** Lincoln Laboratory, Massachusetts Institute of Technology, Lexington, Massachusetts

R**.H.Lipson, Ph.D.** Department of Chemistry, University of Western Ontario, London, Ontario, Canada

Z**henlin Liu, Ph.D.** Hosono Transparent Electro-Active Materials Project, Exploratory Research for Advanced Technology, Japan Science and Technology Corporation, Kawasaki, Kanagawa, Japan

H**.Major, Ph.D.** Department of Physics and Astronomy, Howard University, Washington, D.C.

P**rabhakar Misra, Ph.D.** Department of Physics and Astronomy and the Center for the Study of Terrestrial and Extraterrestrial Atmospheres, Howard University, Washington, D.C.

R**ichard Moncorgé, Ph.D.** Centre Interdisciplinaire de Recherche Ions-Lasers, UMR 6637 CNRS-CEA-ISMRA, Université de Caen, Caen, France

A**.L.Oldenburg, Ph.D.** Department of Electrical and Computer Engineering, University of Illinois, Urbana, Illinois

S**.Paddi Reddy, D.Sc.** Department of Physics and Physical Oceanography, Memorial University of Newfoundland, St. John's, Newfoundland, Canada

L**aurence S.Rothman, Ph.D.** Atomic and Molecular Physics Division, Harvard-Smithsonian Center for Astrophysics, Cambridge, Massachusetts

M**ordechai Rothschild, Ph.D.** Submicrometer Technology Group, Lincoln Laboratory, Massachusetts Institute of Technology, Lexington, Massachusetts

* *Current affiliation:* Department of Physical Sciences, Belfry School, Belfry, Kentucky.

E**vangelia Sarantopoulou, Ph.D.** National Hellenic Research Foundation, Theoretical and Physical Chemistry Institute, Athens, Greece

N**obuhiko Sarukura, Ph.D.** Institute for Molecular Science, Okazaki National Research Institutes, Myodaiji, Okazaki, Japan

Y**.J.Shi** Department of Chemistry, University of Western Ontario, London, Ontario, Canada

R**onald W.Waynant, Ph.D.** Electro-Optics Branch, U.S. Food and Drug Administration, Rockville, Maryland

K**ouichi Yoshino, Ph.D.** Atomic and Molecular Physics Division, Harvard-Smithsonian Center for Astrophysics, Cambridge, Massachusetts

1
Ultraviolet and Vacuum Ultraviolet Sources and Materials for Lithography

Vladimir Liberman and Mordechai Rothschild
Massachusetts Institute of Technology, Lexington, Massachusetts

I. MOTIVATION FOR ULTRAVIOLET LITHOGRAPHY

The relentless drive of the semiconductor industry to smaller device dimensions continues to present new challenges for all the enabling fabrication technologies, and in particular to microlithography. At present, the most advanced microelectronic devices have dimensions of 0.18 μm, and it is expected that these will be reduced further within the next few years to 100 nm and below. The mainstay of mass production lithography has been projection optical lithography, in which the pattern on a photomask is imaged in reduction onto the silicon wafer. From fundamental principles we know that the resolution in such a configuration is directly proportional to the wavelength. Thus, the most straightforward way of reducing printed dimensions is to use radiation sources at shorter wavelengths. Several years ago the industry made the transition from a continuous-wave mercury discharge lamp at 365 nm to a pulsed excimer laser operating at 248 nm (KrF lasers). It is widely expected that in the near future a similar transition will take place to 193 nm (ArF lasers). Beyond that, 157 nm (F_2 lasers) is being explored for sub-100-nm lithography. This shift in lithographic wavelengths from the near-ultraviolet (UV) to deep-UV and eventually to vacuum-UV (VUV) poses new challenges related to optical materials, optical coatings, detectors, and ambient control. This chapter summarizes the key issues encountered at the shorter lithographic wavelengths, and the present state of the art in addressing them.

The definition of the terms "deep-UV" and "vacuum-UV" is not always unambiguous. In lithography "deep-UV" has been applied to 248 and 193 nm, and "VUV" to 157 nm. This chapter will follow this convention: wavelengths in the region 250–190 nm are designated as "deep-UV," and those between 190 and 100 nm as "VUV." The name "vacuum-UV" for wavelengths below 190 nm is a misnomer, since the radiation can propagate in purged ambients as well, such as nitrogen, argon, or helium. The main restriction is that molecular oxygen be absent, since it absorbs strongly in this spectral region (see discussions in Sec. VII). However, even at 193 nm one should avoid the presence of significant amounts of oxygen, because discrete absorption bands do exist there and the atmospheric attenuation can vary from wavelength to wavelength.

II. RADIATION SOURCES

In the deep-UV and VUV spectral regions there exist several radiation sources that can be adapted to specific applications. The main use of such sources in lithography is, of course, for the actual lithographic process (i.e., exposure of resist-coated wafers). However, there are other needs as well: for interferometry, absorption measurements, and at-wavelength inspection of photomasks, among others. The lithographic radiation sources must have high power in order to facilitate a high throughput of the projection systems, and they must be robust, with a low cost of ownership.

The sources that have become the de facto industry standard are excimer lasers. These gas lasers rely on electric discharges to generate the requisite laser population inversion. At 248 nm the radiating species are krypton fluoride molecules. These are formed in their electronically excited state by gas-phase recombination of krypton and fluorine atoms in the presence of a buffer gas (helium or neon). At 193 nm the lasing species are ArF molecules, and at 157 nm they are F_2 molecules. The ground states of the KrF and ArF molecules are dissociative, and therefore a population inversion (and amplified emission) is established as soon as the upper state is populated via collisions. Although this feature makes excimer lasers efficient, it also causes the natural linewidth to be quite broad (a few hundred picometers). In lithography the upper limit on acceptable laser linewidth is determined by the dispersion of the lens materials and by the allowable chromatic aberration of the optical system. For high-numerical aperture optics, the laser linewidth must be narrowed to less than 1 pm [1]. This task is achieved with intracavity optical components such as prisms and gratings. Line-narrowed excimer lasers at 248 and 193 nm are available commercially from several vendors. Their pulse repetition rates exceed 1 kHz and are expected to approach 5 kHz in the near future. Their average power is ~10 W [2,3]. Excimer lasers have a high gain and, therefore, the pulse duration is quite short, typically ~10–20 ns full-width at half maximum. Only few cavity round trips can be generated, and the spatial coherence is consequently low (less than 100 μm correlation length) [4].

The 157 nm laser is slightly different. The lower electronic state of the lasing transition is nondissociative, and, therefore, the natural output spectrum has a discrete structure. It consists of two peaks, each ~1 pm wide, separated by ~100 pm [5]. It is relatively easy to select one of the lines, using intracavity optics, but it is quite difficult to narrow the width of the remaining line to less than ~0.5 pm. In addition, the 157 nm emission of molecular fluorine is accompanied by a red emission (~700 nm) of fluorine atoms generated in the discharge [6]. This red emission is especially noticeable when the buffer gas is helium, and amounts to 3–5% of the total laser power.

Solid-state coherent radiation sources in this spectral range lag significantly behind excimer lasers with regard to power, cost, and reliability. There are no lasers operating in the deep-UV and VUV, but there are schemes for frequency upconversion using Nd:YAG or Ti:sapphire lasers [7]. For instance, the fifth harmonic of a 1.06 μm Nd:YAG laser emits at 213 nm. The nonlinear media required for upconversion are usually crystals such as barium beta-borate (BBO) or lithium borate (LBO). They are transparent to ~190 nm, but their exact transmission at 193 nm, as well as their resistance to laser damage at

this wavelength, are strongly determined by crystalline impurities and defects. The efficiency of the frequency upconversion process into these short wavelengths is less than 10%. Other upconversion schemes do not rely on nonlinear crystals but on the generation of anti-Stokes lines in a gaseous Raman-active medium, or on near-resonant nonlinear processes in certain vapors [8]. At present none of these techniques has been turned into commercially available systems. All of the approaches relying on nonlinear optical processes require high peak powers of a pump laser, and are therefore inherently pulsed sources. They also hold the promise of narrow-linewidth, highly coherent radiation, in contrast with the excimer lasers.

Incoherent sources in the deep-UV and VUV are based on electrical discharges of gases, whether continuous wave (cw) or pulsed. Weak lamps, but covering a broad spectral range, employ low-pressure hydrogen or deuterium molecules. They emit mostly at ~140–170 nm in several rotational-vibrational bands, and they also have weak continua at wavelengths below and above this range [9]. Deuterium lamps are frequently used in spectrophotometers. More intense lamps have limited spectral range. For example, mercury lamps radiate at 254 and 185 nm, corresponding to atomic transitions in mercury. The relative intensity of the 185 nm line varies, since it may be strongly attenuated by absorption in the window material used for the discharge envelope. Other commercially available lamps rely on discharges in xenon (172 nm), krypton (145 nm), or argon gas (126 nm) [10]. The spectra of these are broad, 5–10 nm, and are due to radiative transitions in the respective dimer molecules. The lamp efficiency and its reliability decrease rapidly with wavelength. Therefore, xenon lamps are much easier to obtain and maintain than argon lamps. Their power is nevertheless low compared to that of excimer lasers: it is measured in milliwatts per square centimeter, as opposed to the watts one encounters with lasers. One more wavelength should be mentioned: 121.6 nm. This wavelength of an atomic transition in hydrogen atoms, the so-called Lyman-alpha line, can be obtained quite efficiently in discharges containing hydrogen. Several schemes have been proposed for higher-power 121.6 nm lamps, but they have not yet been demonstrated experimentally.

III. DETECTION OF UV RADIATION

The choice of the detector for the UV region is dictated by several factors related to the incident radiation:

1. Temporal shape of incident radiation and required temporal resolution
2. Incident level of radiation and required dynamic range of the detector
3. Incident wavelength of radiation and required wavelength sensitivity of the detector
4. Durability expectations of the detector

Four types of detectors are commonly used: pyroelectric detectors, thermopiles, photodiodes, and photomultiplier tubes.

The operation of pyroelectric devices is based on a temperature dependence of the electric polarization in certain classes of materials, such as ferroelectrics. Thus, a change in temperature resulting from an incident laser pulse leads to a voltage signal [11].

Pyroelectric detectors are well suited for direct energy and power measurements of excimer laser radiation. For pulsed energy detection, pyroelectric detectors can accommodate fluences as high as hundreds of mJ/cm^2/ pulse and as low as μJ/cm^2/pulse with fast amplifier circuitry. Within this range, three to four orders of magnitude of dynamic range for pulse energy detection can be commonly obtained. For a flat spectral response and efficient energy coupling, the front detector surface may be coated with an absorbing organic paint or a baked-on black ceramic coating. As an alternative, uncoated pyroelectric detectors can be used, whose front surface electrode is a thin layer of chromium. The uncoated design offers the advantage of a much faster detector response for resolving individual pulses at repetition rates above a few hundred hertz; however, the wavelength response is determined by the spectral reflectivity of chromium, and thus can vary by 15–20% across the UV spectrum. When operating pyroelectric detectors in fluence regimens below the material damage threshold, the detector durability is determined by the lifetime of the front coating or a front surface electrode. For instance, in recent tests performed at the Massachusetts Institute of Technology (MIT) Lincoln Laboratory at 157 nm, a commercial pyroelectric detector was observed to fail after 3×10^9 pulses at an incident fluence of 0.5 mJ/cm^2/pulse. The mode of failure appeared to be delamination of the front surface electrode [12].

The pyroelectric response of a detector may be a function of many factors, including crystal size and type, the value of the pyroelectric coefficient, and its dependence on temperature. Therefore, the absolute calibration of pyroelectric detectors is not always straightforward. At present, the National Institute of Standards and Technology (NIST) offers calibration services for pyroelectric detectors at 248 and 193 nm with an accuracy of ±1% [13].

Thermopile devices are useful for measuring continuous wave (CW) radiation sources or average power of pulsed UV radiation. A thermopile consists of an array of thermocouple or thermistor devices that convert incident power into a temperature rise. Because of their simplicity, thermopile probes are considerably less expensive than pyroelectric devices. They can measure intensities from several kilowatts to milliwatts per cm^2. The front surface of a thermopile is typically a black, highly absorptive coating, with a spectral response constant within a few percent over the UV spectral region [14]. The main utility of thermopile probes is the direct determination of incident laser power and laser stability. With NIST calibration, the measurement accuracy can be better than 2% [13]. The most common damage mechanism involves ablation of the black coating. The coating can be reapplied by a detector manufacturer at a nominal cost.

Photodiodes are an excellent choice for detecting highly attenuated pulsed excimer laser radiation when high temporal resolution (better than 1 ns) and wide dynamic range are required. Photodiodes operate on the principle of converting incident photons into electron-hole pairs, which are swept to the opposing ends of a p−n junction, generating current at the device terminals. Diodes for UV applications can be made from a variety of semiconducting materials, including Si, PtSi, and GaP [15]. Photodiodes exhibit excellent linearity over several orders of magnitude: pulsed UV laser energies from under 1 nJ/cm^2 to hundreds of μJ/ cm^2 can be measured. The external wavelength sensitivity of the photodiode is dependent on the surface reflectance, which is a function of the substrate's optical constants. In addition, the internal quantum efficiency of the device increases with

photon energy. The combined effect is a varying spectral responsivity. For instance, for a typical Si-based p−n junction device, a 50% increase in overall sensitivity may be expected as the wavelength is reduced from 248 to 157 nm. Furthermore, as the device ages under UV laser exposure, its wavelength responsivity may change [16].

For metrology applications requiring extremely low-level signal detection, such as transmittance, reflectance, and ellipsometry measurements in the ultraviolet, photomultiplier tubes (PMTs) offer the best solution. In a popular configuration the PMT window is coated with a fluorescing material, such as sodium salyci-late. Ultraviolet light striking the sodium salycilate will cause it to fluoresce at a wavelength of approximately 400 nm, which can in turn be detected by a PMT designed for the visible spectral region [17]. For ultimate detection of low signals, UV-sensitive solar-blind PMTs are used. These have photocathodes insensitive to visible radiation, such as CsI or CsTe. PMTs have constant responsivities over thousands of hours when used with low-level CW radiation. They are not generally used for measuring pulsed UV laser radiation since both sodium salycilate and photocathode materials can be easily damaged with high peak powers.

IV. UV OPTICAL METROLOGY

A. Bulk Materials

In discussing UV optical metrology relevant to microlithography, it is convenient to classify the topic into two parts: measurement of bulk material properties and surfaces, and measurement of thin film properties. Bulk materials relevant to UV microlithography would include lens materials, such as fused silica, single crystal fluorides (calcium fluoride, barium fluoride, and others), and photomask materials, such as fused silica. For lens materials, important optical properties include transmission and loss at the lithographic wavelength, and highly accurate refractive index values. The transmission and optical losses of the lens materials have immediate impact on the overall system transmission and throughput. Furthermore, residual absorption causes lens heating, which, through the temperature dependence of the index of refraction, can cause unacceptable lens aberrations. An accurate knowledge of the index of refraction, its temperature dependence, and its dispersion is essential to the design and tolerancing of near-diffraction limited optics such as those used in lithographic systems.

The transmission and maximum loss requirements are a sensitive function of a particular lens design. For 193 nm and 157 nm applications, a consensus [12] has been developed that acceptable losses in a bulk material should not exceed 0.5%/cm at the wavelength of use, which is expressed as a maximum bulk absorption coefficient of 0.002/cm, base 10.

When prescreening optical materials, one must separate bulk losses, such as bulk absorption and scatter, which are intrinsic to the material, from surface losses, which are a function of surface polishing and ambient conditions. For a sample of length l the internal transmission is:

$$T_{int}=10^{-[2\beta+(\alpha+\gamma)l]} \tag{1}$$

where β refers to the loss of a single surface, including absorption and scatter; α is the internal absorption coefficient per unit length; and γ is the bulk scatter coefficient per unit length [18]. Experimentally, one measures the external transmission, which includes the internal transmission as well as surface reflections due to index mismatch (Fresnel losses). The internal transmission can then be approximated by:

$$T_{int}=T_{ext}(n+1)^4/(16n^2) \tag{2}$$

where n is the refractive index of the material. The procedure for obtaining bulk losses involves measuring the transmission of several samples of different lengths, all with the same nominal surface finish. Then, applying Eqs. (1) and (2) above, one derives α+γ. In order to obtain the bulk absorption coefficient, separate bulk scatter measurements must be performed. Additional metrology complications may arise because the material characteristics can change in the course of laser irradiation: surface losses may change due to laser cleaning or contamination and bulk losses may vary due to laser induced bleaching or absorption. Thus, when long-term irradiation experiments requiring a high degree of accuracy are needed, it is desirable to irradiate several samples of the same grade and different lengths simultaneously.

Because of the expected high initial transmission of lens materials, samples at least several centimeters in length need to be measured to obtain appreciable loss signals. Commercial spectrophotometers are not well suited for measuring longer samples. This is due in part to the limited length of the sample compartment, and in part is a result of the high divergence of the spectrometer beam. From our experience at MIT Lincoln Laboratory, the above issues can cause transmission measurement errors >2% for an 8 cm-long sample at wavelengths below 200 nm. This measurement discrepancy of >0.25%/cm is a significant fraction of the specification of initial material transmission.

An alternative, more accurate, and precise technique of transmission measurements of long bulk samples utilizes an excimer laser light source. This technique is especially useful in conjunction with long-term materials durability studies, since transmission measurements can be performed in situ [18]. A typical measurement setup (Fig. 1) involves using a beamsplitter before the sample to reflect part of the incident beam onto a reference detector. The main part of the laser beam is incident on the sample detector, which is positioned directly behind the sample station. Measurements are obtained ratiometrically. For the incident laser fluences of interest (from 0.1 to 10 mJ/cm^2/pulse), pyroelectric detectors are well suited to the task of transmission measurements. Most material evaluation studies for UV lithographic lens applications are performed using the laser ratiometry method described above, whether they are carried out by the material suppliers, by independent laboratories, or by lithographic lens manufacturers. In using pulsed laser ratiometry for in situ single-wavelength transmission measure-

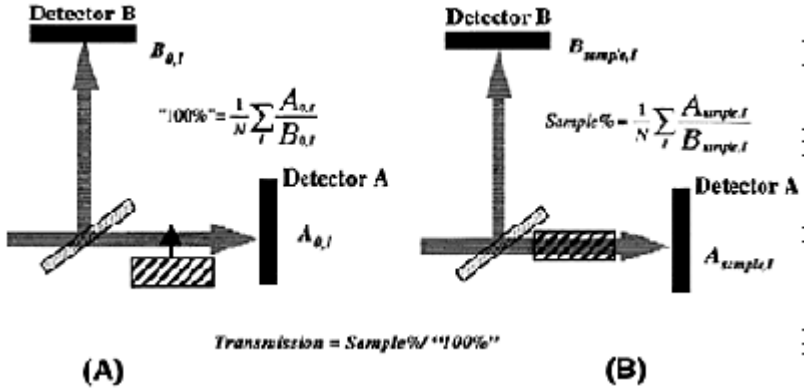

Figure 1 Schematic representation of an in-situ laser-based transmission measurement scheme. A. Measurement configuration for obtaining "100%" transmission. B. Measurement configuration for obtaining sample transmission.

ments, one must be careful to separate potential two-photon absorption from linear absorption. The total absorption coefficient is

$$\alpha_{tot}=\alpha_0+\beta I \tag{3}$$

where α_0 is the linear absorption coefficient, β is the two-photon absorption coefficient, and $\boldsymbol{I}$ is the peak intensity of the laser pulse. The two-photon absorption coefficient can be obtained by plotting the total absorption coefficient as a function of incident peak intensity and obtaining the slope of the linear regression. Typical two-photon absorption measurements for either fused silica or calcium fluoride at 193 nm yield β=0.5−1 cm/GW (base 10) [19–22]. For a pulse width on the order of 10 ns and a fluence of 10 mJ/cm^2/pulse, $\beta\boldsymbol{I}$=0.0005–0.001/cm (base 10), compared to the specification of α_{tot} less than 0.002/cm (base 10). Thus, in order to keep the effect of two-photon absorption below ~25% of the total measured value, fluences below 10 mJ/cm^2/pulse should be used in laser ratiometry.

Microlithographic projection systems are designed to have near-diffraction limited performance, with very small wavefront aberrations. Their design is sensitive to the exact value of the lens material's index of refraction, which must be known to within 10 ppm. The most accurate measurements to date of the index of refraction of materials transparent in the UV region have been obtained by the minimum deviation method [23].

B. Thin Films

Accurate knowledge of the optical properties of thin films is important to many areas of microlithography. For instance, a lithographic lens manufacturer may want to develop a variety of multilayer thin film coatings applied to lens surfaces that will either eliminate surface reflections or allow the element to reflect a prescribed amount, depending on the particular lens design. Although the principles of designing such thin film coatings are well understood, the optical properties of the constituent layers often are not. This lack of information has hampered the development of high-performance coatings in the UV wavelength range.

Many lithographic applications require knowledge of the refractive index and absorption coefficients of thin films, in addition to reflection and transmission data. For instance, knowledge of the refractive index of thin films for lens coatings is needed for precise coating designs. Another application is the tailoring and modeling of photoresist performance, which require knowledge of the optical constants of resists and their constituents (such as photoacid generators). Similar data are needed for the optimization of bottom antireflectance coatings (BARCs), which are applied to the wafer surface prior to the deposition of photoresists to suppress back reflections into the resist. The extraction of optical constants of thin films is best performed with ellipsometry, as discussed in Sec. IV.B.2 below.

1. Transmittance and Reflectance Measurements

For the lifetime testing of optical coatings, accurate spectrophotometric reflectance and transmittance measurements need to be performed periodically. The stringent demands of the material's durability impose strict requirements on the measurement reproducibility. For instance, for durability studies of antireflectance coatings and high reflector coatings, both transmission and reflectance over the UV spectral range may need to be recorded over periods of months with repeatability around 0.1%. In addition, it is not sufficient to record single-wavelength data that are available with a laser-based measurement (as is the case with bulk materials), since useful information about degradation mechanisms of coatings can be learned only from their full spectral behavior.

Transmission and reflection measurements in the near-UV spectrum can be performed to high accuracy and precision, but special challenges arise for metrology below 200 nm. Both water vapor and oxygen absorb strongly in this wavelength region and therefore the instruments must either be purged with a transparent gas or operated under vacuum. The ambient constraints complicate the instrument design, and significantly increase the times needed for sample transfer and measurement. All the transmitting windows, bulb envelopes, and photomultiplier windows must be made either of UV-grade synthetic fused silica or, for operation below 180 nm, of magnesium or calcium fluoride. If polarizing elements are needed in the VUV, the most common option is Rochon prisms made of optically contacted magnesium fluoride elements. They are designed to deflect the extraordinary ray by several degrees while letting the ordinary ray pass straight through.

A simple VUV spectrometer design utilizes a ratiometric method to normalize bulb

intensity fluctuations during a wavelength scan. In that configuration, light from a monochromator is incident on a beamsplitter, where a part of the beam is deflected onto a reference detector and the rest of the beam is used for sample transmission measurement. By contrast, in a dual beam-single detector system the two beams are formed using a chopper wheel. During a wavelength scan, for every chopper cycle both a reference and a signal scan are obtained. The technique produces a superior signal-to-noise ratio. The dual beam-single detector designs are quite common for near-UV and visible spectrometers, but they have only recently been incorporated into VUV spectrometers.

In addition to the challenges inherent in obtaining precise readings in the deep-UV, accuracy is difficult to achieve since there are no primary transmission or reflection standards in this wavelength range. The difficulty in developing such standards in the deep-UV stems from the fact that the optical properties of materials are not known with sufficient accuracy, and surface losses due to polishing or surface contamination can significantly influence measurements below 200 nm (see Sec. VII) [24]. Therefore, standards for sample preparation and surface treatment need to be established as part of every measurement procedure. The impact of surface cleaning on the transmission and reflection measurements has only recently been assessed, and a considerable amount of work must be performed before reliable transferable standards are developed.

Several specular reflectance configurations for high accuracy and precision measurements have been successfully implemented in the deep-UV and VUV. Integrating spheres, while popular at longer wavelengths, are not practical below 200 nm because of the lack of a suitable coating reflector material. In the absence of reflectance standards for the VUV range, one needs to use self-referencing schemes, including goniometer-based measurements and use of absolute reflectance accessories, such as V-W and V-N methods. In the latter, the nomenclature describes the beam path traced by a light beam in the baseline and reflectance measurement positions, respectively. The advantage of goniometer over fixed-angle setups is an ability to measure a wide range of specular reflectance signals. However, this arrangement is not compatible with so-called straight-through single-detector spectrometers. For the single-detector schemes, V-W and V-N methods can be used (Fig. 2). Both methods utilize movable mirrors to ensure that, for both baseline and reflectance measurements, the same number of mirrors direct the light beam and the path length is identical for both baseline and sample measurements.

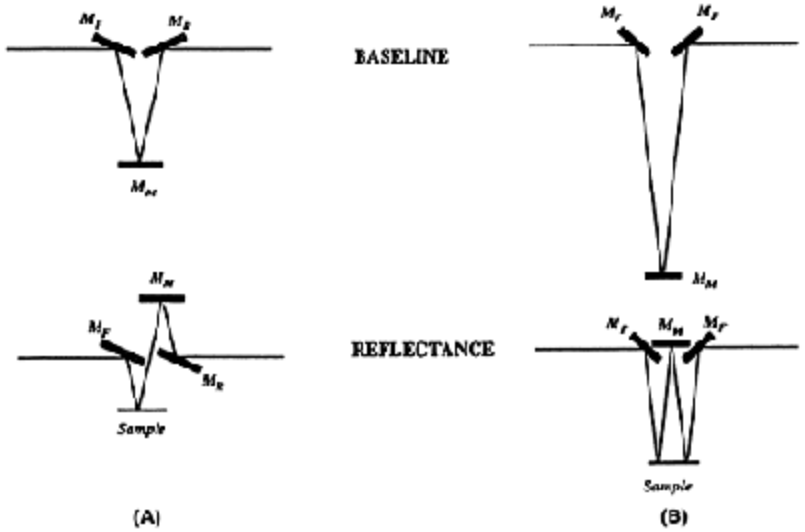

Figure 2 Geometric representations of V-N (A) and V-W reflectance (B) methods. M_F, fixed mirror; M_R, rotatable mirror; M_M, movable mirror.

2. Ellipsometry

Although accurate measurements of reflection and transmission of thin films, as described above, can be used to extract the material optical constants [25], variable angle spectroscopic ellipsometry (VASE) is better suited for such purposes. Ellipsometric parameters relate to a ratio of two reflectivities of different polarizations; thus, the measurements are self-normalizing. Additionally, the phase change upon reflection, obtained in ellipsometric measurements, is sensitive to the presence of very thin films and to the interface structure and therefore can yield valuable information in these areas [26,27]. The extension of VASE to VUV encounters certain practical challenges, similar to those discussed above in the context of spectrophotometry: sources, coating and window materials, polarizers and detectors need to be engineered or optimized for this wavelength range. Ellipsometers must work in a purged or vacuum ambient; thus, instrument access is limited, and automation of the alignment procedure must be engineered. Significant progress has been made recently towards the design of purged UV VASE, and commercial systems are now available with comparable performance to that obtained in the near-UV [28,29].

V. OPTICAL MATERIALS

There is a limited choice of optical materials in the deep-UV and VUV that would both meet the initial requirements of the excimer-laser based lithographic sy stems and exhibit the required lifetime durability. For instance, some materials with excellent damage resistance, such as crystalline quartz, magnesium fluoride, and sapphire, are intrinsically birefringent and are thus unsuitable for a lithographic system that is polarization-sensitive. Coupled with the initial requirements of low birefringence, candidate materials must exhibit excellent index homogeneity and must be available in sufficient quantity to meet the demand of the semiconductor industry. The only practical materials that could meet the preceding requirements are amorphous fused silica and crystalline fluorides, primarily calcium and barium fluorides.

A. Fused Silica

The fused silica used in UV lithography applications is of very high purity. All the trace element impurities are in the sub-100 parts per billion (ppb) level. Hydroxyl groups and hydrogen are present in various amounts in 193 nm and 248 nm grade fused silica, because they apparently improve the resistance of fused silica to laser induced damage. Fused silica for 157 nm applications is somewhat different: since OH absorbs at this wavelength, the material must be "dried." Instead of the hydroxyl groups that are removed, fluorine atoms are added to the network. This process extends the transmission edge of the fused silica to below 157 nm, since fluorine titrates absorbing defects and dangling bonds.

The high-purity fused silica represents an atomic structure very close to the ideal continuous random network, comprised of perfect $Si(O_{1/2})_4$ tetrahedra (Fig. 3A) joined at the corners with statistically determined Si–O–Si and dihedral angles [30,31]. In an amorphous fused silica the tetrahedra form closed rings with varying numbers of members, from three tetrahedra and up (Fig. 3B).

Modeling the absorption band-edge of fused silica by an Urbach rule for near band-edge absorption by excitons [32] predicts a lower absorption limit of $\sim 10^{-5}$/cm at 193 nm. However, the most transparent fused silica that has been measured exhibits much larger absorption coefficients, in the range of 10^{-3}/cm. This discrepancy between expectation and experiment indicates that the transparency of fused silica in the deep UV is limited by defects, whether intrinsic or radiation-induced, by OH impurities, and by bulk scattering (Fig. 4) [30].

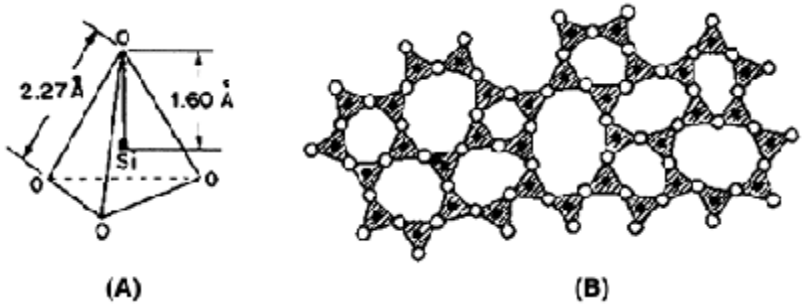

Figure 3 A. Basic structural unit of silicon dioxide. B. Two-dimensional representation of the amorphous fused silica. (From Refs. 30, 31.)

Several types of lattice defects contribute to the deep-UV absorption of fused silica. One is the nonbridging oxygen hole center, the spectral signature of which is an absorption band at ~4.8 eV (260 nm). This defect can be represented by the notation ≡Si–O·, where the three parallel lines represent three separate bonds to oxygen atoms, and the dot represents an unpaired electron. The width of the band is broad enough to overlap the 248 nm excimer laser line. However, this defect does not contribute to absorption at 193 nm and below.

The second defect, the E′ center, can be represented by the notation ≡Si·, and refers to an unpaired electron on a silicon atom. The absorption band caused by this defect is centered at 5.8 eV (215 nm) and is broad enough that it overlaps the 193 nm laser line. The laser-induced formation of E′ centers is believed to be the dominant cause of the observed degradation in deep-UV transmission when fused silica is irradiated with 193 nm lasers.

Scattering-induced transmission losses in fused silica arise from statistical density fluctuations. The general form of this scattering loss, γ, can be expressed by [33]

$$\gamma \propto (n^8/\lambda^4)p^2T_f\beta_T \tag{4}$$

where n is the refractive index, λ is the wavelength, p is the photoelastic constant, T_f is the fictive temperature, and β_T is the isothermal compressibility at T_f. The contribution of the bulk scattering losses in the deep-UV can be extrapolated from total integrated scatter measurements performed in the near-UV and visible, using the expression above to correct for wavelength and dispersion effects. From those measurements, a bulk scatter loss of $\gamma \approx 10^{-3}$/cm at 193 nm has been derived [18]. Thus, for the high-purity fused silica, bulk scatter is comparable to absorption from intrinsic defects.

The most critical optical elements in a lithographic system are those forming the projection optics. It is expected that in a manufacturing environment they

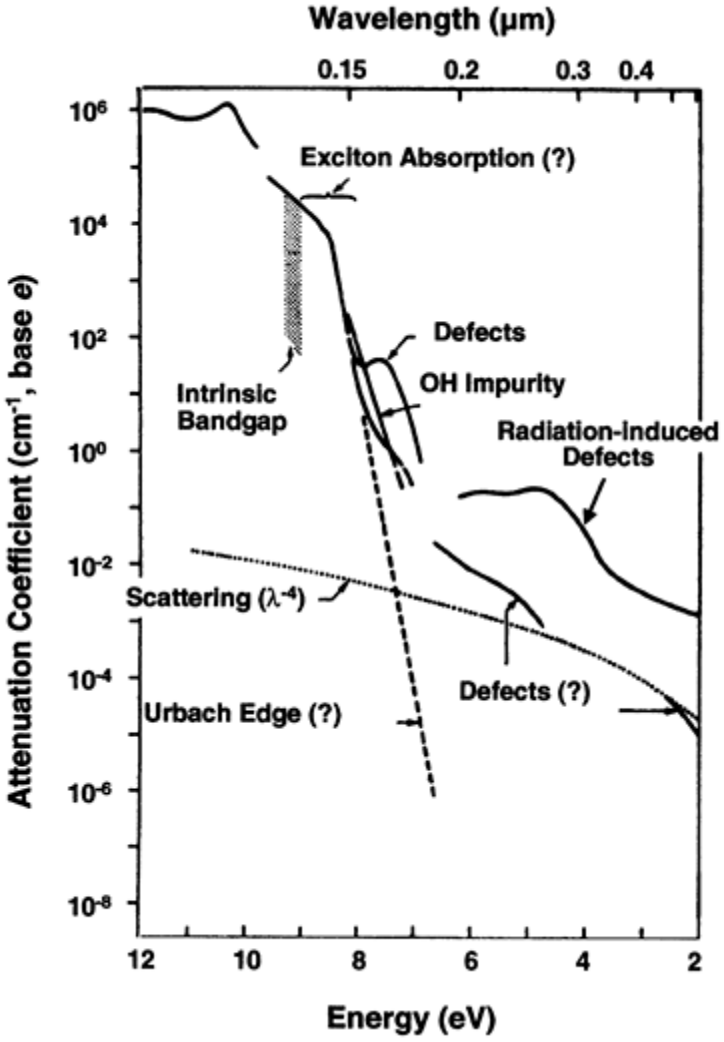

Figure 4 Attenuation coefficients of amorphous fused silica as a function of wavelength and energy. (From Ref. 30.)

will be exposed to fluences up to ~0.1 mJ/cm^2/pulse for 4–10×10^9 pulses per year. The fluences are low enough that the electric fields are orders of magnitude below the threshold for dielectric breakdown in fused silica. They are also low enough that, coupled with the low absorption coefficient, the induced temperature rise is only a few degrees even at high pulse repetition rates. Therefore, any laser-induced changes are not caused by either breakdown or thermal effects. Instead, there may be small photo-induced processes whose cumulative effect is noticeable only after large pulse counts. Several laser-induced phenomena in fused silica have been reported, but their mechanistic details

and even their scaling laws are not yet fully understood. It has been previously observed that 248 nm irradiation at higher fluences of initially transparent fused silica causes a sudden drop in transmission after a few million pulses, a phenomenon termed strong absorption transition (SAT) [34]. This effect has not been documented with lasers below 248 nm, nor has its fluence scaling been reported. Other changes that occur in fused silica after prolonged irradiation are a gradual loss in transmission and a laser-induced structural rearrangement of the fused silica network, which can manifest itself as densification. All the above phenomena adversely affect the performance of optical systems by changing either their transmission or their effective optical path length.

Our description of irradiation-induced damage of fused silica will be structured in two parts: high-dose damage studies of fused silica for 193 nm lens materials applications, and lower-dose irradiation studies of modified (fluorine-doped) fused silica for 157 nm photomasks. The behavior of fused silica at 248 nm is qualitatively similar to that at 193 nm but the damage rates are about one order of magnitude smaller.

1. Fused Silica for 193 nm and 248 nm Applications

Most earlier reports of UV laser-induced damage to bulk fused silica are based on studies performed at fairly high fluences (10^2 mJ/cm^2/pulse) pulse counts (on the order of 10×10^6 pulses) [31,35–46]. More recent damage studies of fused silica are specifically aimed at understanding degradation effects relevant to microlithography (i.e., those observed in the lower-fluence, higher pulse count regimes) [18,47–51]. At MIT Lincoln Laboratory we surveyed 10 grades of fused silica from six commercial suppliers designed for 193 nm [50]. All were designated as lithographic grade. To increase the pulse accumulation rate the irradiation test bed used 193 nm radiation from two free-running 400 Hz excimer lasers, achieving an effective 800 Hz pulse repetition rate. The incident laser beams were temporally interleaved and spatially overlapped by a 50/50 beam splitter and subsequently distributed along 12 beamlines to deliver an incident laser fluence in the range 0.25–4 mJ/cm^2/pulse. More than 100 different samples were tested. For the material with the highest transmission, lifetime durability tests were extended to pulse counts on the order of 10^9.

The details of material growth were not made available, in order to protect the suppliers' confidentiality. The study aimed instead to assess the state of fused silica as it applies to serving the needs of the lithographic community by deriving general trends in degradation behavior and analyzing the spread among various grades.

I*nduced Absorption.* For the samples tested, the initial 193 nm bulk absorption coefficient was found to vary from 0.001 to 0.01/cm (base 10), depending on the grade tested. The majority of the samples had initial absorption coefficients below 0.002/cm (base 10), which is a target value for maximum acceptable absorption derived in consultation with lithographic lens manufacturers. Upon irradiation, several different trends were observed (Fig. 5). Most samples displayed varying degrees of transmission recovery at the onset of irradiation. Depending on the amount of recovery, this phenomenon could be either laser-induced surface cleaning (1–2% total per sample, length-independent) or bulk bleaching (up to 2% per cm, scaling with sample length). Thereafter, the 193 nm absorption coefficients were found either to reach a plateau or

exhibit slow continuous growth. No SAT phenomenon was observed for any sample for the largest doses exposed (5×10^9 pulses at 1 mJ/cm^2/pulse).

In general, the details of the degradation mechanism of fused silica under low-level irradiation can be a fairly complex function of small amounts of impurities in the glass, such as OH and H_2. A recent study has correlated the degree of damage under similar irradiation condition to the amount of hydrogen dissolved in the glass network [48]. The time-dependent absorption behavior has been modeled as an interplay of two competing processes: activation of preexisting defects into E′ centers by incident photons and quenching of these defects by dissolved hydrogen to form nonabsorbing SiH bonds [48].

Figure 5 193 nm absorption coefficients of several grades of fused silica as a function of a number of laser pulses (in millions). The incident fluence is 1 mJ/cm^2/pulse. (From Ref. 50.)

The absorption measurements shown in Figure 5 represent a permanently induced absorption. However, fused silica also exhibits a temporary reduction in transmission following initial exposure to laser irradiation, and a partial recovery in transmission once the laser is turned off [40,48,52]. Typical time resolved absorption data for a fused silica sample are shown in Figure 6. [53]

L*aser-Induced Structural Changes: Densification and Rarefaction.* It has been reported for several decades that, when exposed to prolonged low levels of ionizing and nonionizing radiation, fused silica undergoes densification, as manifested by an increase in its refractive index in the irradiated area. This phenomenon has been observed to occur also with the subbandgap irradiation of excimer lasers. The somewhat indirect observations of densification are small, typically a few parts per million (ppm). Because of their magnitude it has not been possible to obtain direct evidence of the structural rearrangement of the lattice or the density increase. Interferometric measurements of wavefront retardation or measurements of stress-induced birefringence through the photoelastic effect are used instead to measure the amount of densification. Nevertheless, the impact of material densification, even in the ppm range, on the performance of a

high-quality lithographic system can be devastating, causing unacceptable wavefront aberrations. Over a lens lifetime, it is estimated that a maximum of 1 ppm densification may be tolerated.

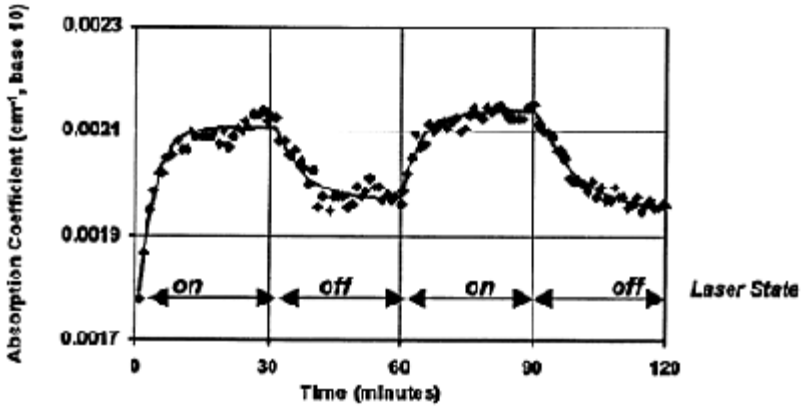

Figure 6 Temporal behavior of 193 nm fused silica absorption as the incident laser is turned on and off. Data shown are obtained for an 8-cm long sample at an incident fluence of 0.25 mJ/cm^2/pulse. (From Ref. 53.)

It has been proposed that UV laser-induced densification follows a power law. If N is the pulse count and the fluence is Φ, then the fractional densification δ is

$$\delta = k(N\Phi^2/\tau)^x \tag{5}$$

where k and x are empirically derived constants, with x typically between 0.5 and 0.8, and τ is a measure of effective laser pulsewidth, assuming that a two-photon effect is operative [54]. This power law has been confirmed experimentally in long-term studies performed at MIT Lincoln Laboratory and elsewhere [19,39,50,51,55,56]. The irradiation was typically with unpolarized light, at fluences of <0.5–100 mJ/cm^2/pulse, and for pulse counts up to 5×10^9. Some of these studies reported that k and x as defined in Eq. (5) varied somewhat between grades and with incident fluence levels.

To extend the applicability of the densification scaling to the lifetime doses of lithographic tools ($40–100\times10^9$ pulses at 0.1 mJ/cm^2/pulse), an ultramarathon irradiation study has been recently performed [57]. It used time-delay pulse multiplexing of a 2 kHz lithography-grade 193 nm laser beam for an effective operating rate of 8 kHz. The study used polarized light and periodically assessed both interferometric wavefront distortion and stress-induced birefringence of the irradiated fused silica samples. Rather than showing conventional densification through increase in the optical pathlength, the study revealed the opposite effect: rarefaction. The magnitude of this effect was about 0.5 ppm/cm after 40×10^9 pulses. Early studies of fused silica did detect expansion under ionizing irradiation [58–60], but this is the first demonstration of such a phenomenon

with UV laser light. The accompanying birefringence signal did not suggest a development of a symmetrical stress field that would be induced by a round laser spot, but exhibited anisotropy that seemed to be induced by the linear polarization of the laser. While at present the laser-induced rarefaction phenomenon is not well understood, it is clearly relevant to attempts to predict the practical lifetime of lithographic lens optics.

2. Modified Fused Silica

Even the highest-quality 193 nm fused silica is not transmissive enough at 157 nm. However, in the last year significant progress has been made to improve its transmission substantially in the 155–175 wavelength region by modifying its composition [61,62]. The general approach consists of two steps: reduce the hydroxyl content of fused silica, since the OH moieties absorb at wavelengths above about 175 nm; and introduce fluorine into the glassy network, in order to titrate all the unpaired electrons on the silicon atoms. Figure 7 shows the transmission of conventional UV-grade fused silica and modified fused silica [63]. The transmission of a 1 cm thick modified fused silica is about 82% at 157 nm, as measured

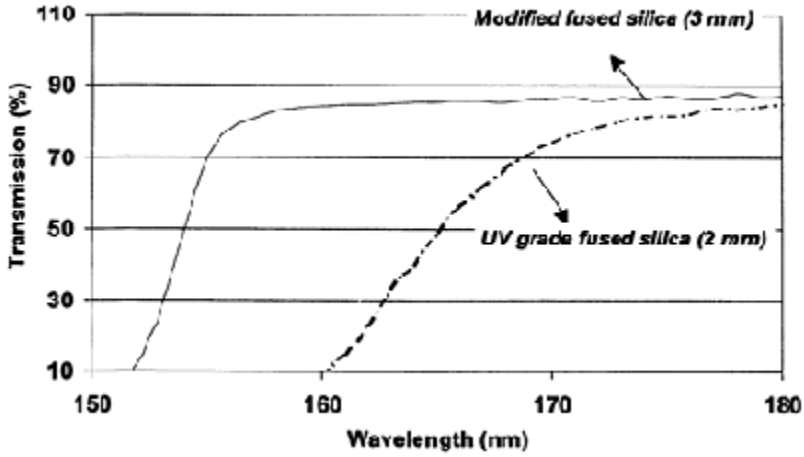

Figure 7 Transmission comparison of standard UV grade fused silica (dot-dash) and a modified fused silica (solid line) samples.

in a vacuum-UV spectrometer. This value should be compared to the theoretical maximum of 88%, obtained from the index of refraction and by allowing for only Fresnel reflection losses. It thus appears that there still is a residual absorption of ~6% in the sample measured. In fact, 3–4% losses can be attributed to surface losses that are removed under laser radiation. The intrinsic absorption coefficient of the modified fused silica can be as low as 0.02/cm (base 10) at 157 nm.

The primary application of modified fused silica is as a transmissive substrate for photomasks at 157 nm. The requirements for good mask material are more relaxed than those for lens materials. High initial transmission needs to be ensured only for a 6 mm

thickness (the standard mask thickness), and lifetime requirements must be met only for ~60×10^6 pulses at 0.1 mJ/cm^2/pulse. Several modified fused silica samples were evaluated at MIT Lincoln Laboratory, and some met the criteria for low initial absorption as well as for stable transmission at the pulse counts and fluences listed above [12].

B. Calcium Fluoride

The lattice structure of crystalline calcium fluoride is shown in Figure 8. Each fluoride ion is tetrahedrally bound to four calcium ions. Calcium fluoride has excellent transmission down to 130 nm. It is inert, has very low water solubility, and can be grown in large-diameter boules. Because of its excellent resistance to high-power laser irradiation, the material has found extensive use in illuminator

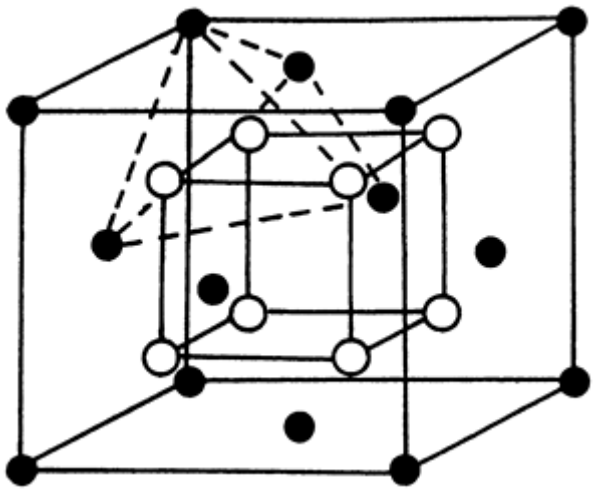

Figure 8 A unit cell of calcium fluoride. Light balls, F^- dark balls, Ca^{2+} ions.

designs for 193 nm lithographic systems. The growth in material processing and polishing infrastructure has positioned CaF_2 as the primary candidate for lens materials for 157 nm lithography as well.

Early studies assessing transmission and radiation-induced color centers in undoped calcium fluoride had difficulties separating impurity-induced from intrinsic defects [64–66]. Nevertheless, the most often seen intrinsic color centers are the F center, a single electron trapped in a fluorine vacancy; and the M center, an aggregate of two nearest F centers. The absorption peak of the F band is at ~380 nm, while the M center is dichroic with the two main peaks at 360 nm and ~550–600 nm (see Fig. 9). Since the intrinsic color centers are sufficiently far from 193 nm, the transmission properties at that wavelength and at 157 nm are limited by impurities in the material. In fact, long-term low-fluence 193 nm durability studies of calcium fluoride showed that the initial absorption first increases and then saturates [18]. Similar long-term studies under 157 nm irradiation revealed no added 157 nm absorption for pulse counts in excess of 1×10^9

[12,63]. Although considerable variations exist among calcium fluoride suppliers, total absorption coefficients (initial plus laser induced) of less than 0.003 cm^{-1} (base 10) can be readily obtained for a number of materials at both 193 and 157 nm wavelengths.

Due to its single-crystal nature, calcium fluoride does not undergo radiation-induced density changes such as those observed in fused silica. Furthermore, bulk scattering in the material is at least an order of magnitude less than that of fused silica. The main challenges in producing CaF_2 for lithographic lens applications include the ability to grow large-diameter crystals (>200 mm) with no dislocations, perfect crystallinity over the full open aperture, low stress-induced

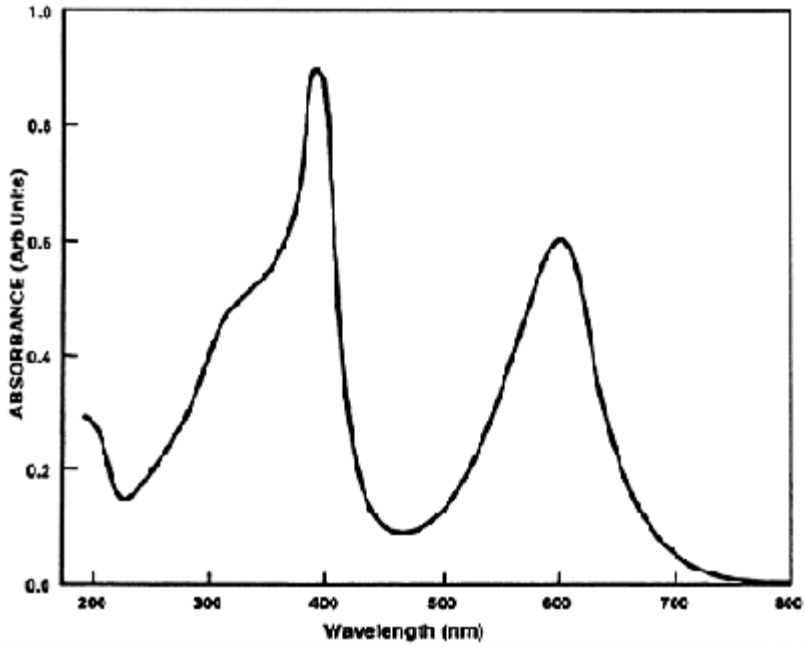

Figure 9 Color centers in CaF_2 induced by 193 nm irradiation.

birefringence (<1 nm/cm at 633 nm), and good index homogeneity (better than 1 ppm at 663 nm).

C. Other Fluorides

For projection lens systems utilizing an all-refractive optical design, a second lens material would be required to provide achromatization across the spectral bandwidth of the 157 nm excimer laser (≈1 pm). The second material option is being pursued in addition to engineering the lasers to bandwidths below ≈0.5 pm. Such second refractive lens materials must meet the same stringent requirements as CaF_2: transmission, durability, index homogeneity, low stress birefringence, among others. The material should also have good mechanical, thermal, and environmental stability.

Table 1 summarizes key properties of several potential material candidates.

Table 1 Relevant Properties of Potential Lens Materials for 157-nm Lithography

Material	Refractive index at 20°C	Index dispersion, dn/dλ (/nm)	*dn/dT* in N_2 (ppm per °C)	OPD ($\times 10^{-6}$/deg)	Thermal Conductivity (W/m/K)	Comments
CaF_2	1.559	−0.0026	8	12	9.7	Primary choice for lens material.
Modified SiO_2	1.654	−0.0050	39	24	1.4	Marginal absorption (>0.02/cm), long-term radiation durability appears satisfactory.
LiF	1.486	NA	0–4	12–15	11.7	Optical quality, radiation durability, polishing may pose challenges.
SrF_2	1.576	−0.0031	9	12	8.5	Index dispersion is marginally different from that of CaF_2.
BaF_2	1.657	−0.0044	10.6	13.6	7	Index and dispersion complement CaF_2. Transmission and laser damage must be further tested. Prone to thermal shock.

All wavelength-dependent data are at 157.6 nm. All material properties are from Ref. 67, with the exception of LiF, which is from Ref. 69.

All the materials listed are nonbirefringent and are expected to have good transmission properties at 157 nm. The optical pathlength difference (OPD) shown in Table 1 is defined as

$$\mathrm{OPD}=1/n[(n-1)\alpha+dn/dT] \tag{6}$$

where α is the coefficient of thermal expansion. The highest-performing modified fused silica has transmission somewhat inferior to that of single crystal fluorides. It also has a thermal conductivity about an order of magnitude lower than that of fluorides, resulting in a higher temperature rise per unit incident laser flux. Its OPD per degree is the highest of the materials listed because of its high thermooptic coefficient *dn/dT* at 157 nm. These disadvantages, in addition to marginal initial transmission, would limit the use of modified fused silica to very few elements in an optical train. Of the remaining materials listed, barium fluoride is the best candidate. It has sufficiently different dispersion from that of calcium fluoride to enable achromatization over ~1 pm [67], high thermal conductivity, and good radiation durability when exposed to gamma rays [68], and in initial 157 nm durability testing [12,63]. However, an infrastructure for growing large sizes of this material still needs to be developed. Techniques for polishing and figuring of this material to the required tolerances have not yet reached maturity, nor have low-stress birefringence and index inhomogeneity been demonstrated.

Strontium fluoride has optical properties intermediate between those of calcium fluoride and barium fluoride. In recent 157 nm tests it showed promising initial transmission and laser durability results [12]. However, refractive index and dispersion measurements performed at NIST [67] suggest that the index dispersion of SrF_2 may not be sufficiently different from that of CaF_2 to warrant its use as a second refractive material. Thus, there is not likely to be a strong demand for strontium fluoride for UV lithographic applications.

VI. OPTICAL COATINGS

Dielectric coatings applied to lithographic elements can be classified into three main categories: antireflective designs for throughput enhancement and ghost image suppression, high reflectors for beam steering purposes; and partial reflectors/beamsplitters employed primarily in catadioptric designs. The coating stacks will consist of layers of alternating high- and low-index materials, as compared to the substrate index. The layers must be transparent enough at the wavelength of use to enable an efficient design and to ensure good damage resistance. For 157 nm lithography the choice of coating materials will be primarily limited to fluorides, since most oxide compounds are too absorptive. For instance, low-index materials may include magnesium and aluminium fluorides, while high-index materials may include lanthanum and gadolinium fluorides. For 193 nm the choice of materials is more relaxed; oxides may also be used, in addition to fluorides. Therefore, the oxides of aluminum, hafnium and zirconium may also be considered as high-index candidates, while for low-index materials silicon dioxide is a possible choice.

In addition to the optical properties of the materials used in thin film coatings, the microscopic structure of the films plays an important role. Thin films tend to be more porous than bulk materials, and airborne molecules may adsorb onto the surfaces of the micropores. It was previously observed that water can incorporate into thin films, thus changing their effective index of refraction and thereby shifting the optical response of multilayers. This effect occurs even at wavelengths at which water is transparent (400–

700 nm) [70], and it would be even more pronounced below 180 nm, where water also absorbs radiation. This effect may be mitigated by increasing the film deposition temperature, since the packing density changes from ~70% at room temperature to over 90% at 300°C [71]. However, higher deposition temperatures are not always practical because of thermally induced stresses at the substrate-coating interface. For UV applications, both water and hydrocarbon contamination need to be considered in their effect on coating layers. Although condensed water is nearly transparent above 200 nm, it does absorb significantly in the VUV range. The absorption coefficient of condensed water is 7/μm (base 10) at 157 nm. Hydrocarbons have strong absorption throughout the UV range, depending on their molecular structure.

Even small amounts of water adsorption can have significant effects on the performance of multilayer coatings in the VUV range. By way of example, we have modeled the effect of 1% moisture incorporation into coating layers for a LaF_3/MgF_2 system designed for 157 nm [63]. The simulations (Fig. 10) show that even such a modest amount of water can cause a drop of 2% in the transmittance of an antireflective design and in the reflectance of a high-reflectance system. By comparison, for a design centered at 193 nm, where the absorption coefficient of water is $<1\times10^{-5}$/μm, a change of less than 0.2% is observed for either an antireflective or a full reflector stack.

A. COATINGS DURABILITY STUDIES

Laser-induced coating damage has received a large amount of attention in recent years because of high-power laser optics applications [42,72–75]. Most studies involved the determination of laser-induced damage thresholds (LIDTs) using so-called one-on-one or S-on-one measurement techniques. The former method is a measurement of energy required to produce damage to a coating in a single laser pulse. The latter involves a determination of a maximum laser pulse energy that a coating can withstand for a fixed number of pulses, usually a few tens to a few hundreds. Typical one-on-one LIDT thresholds for dielectric coatings in

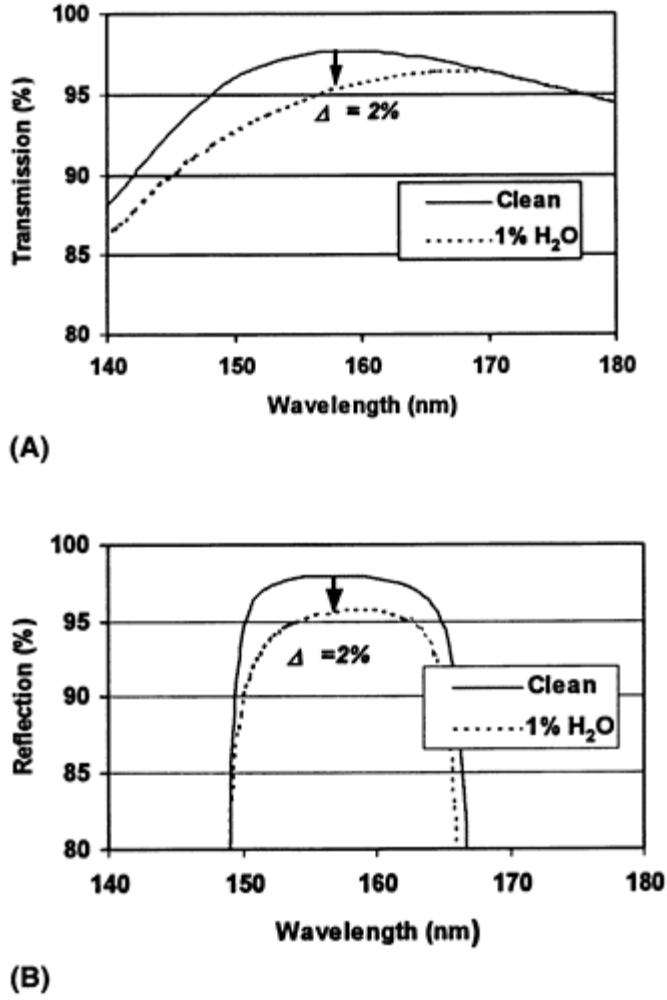

Figure 10 Effects of 1% moisture incorporation into thin film dielectric layers on (A) transmission of a three-layer antireflectance coating and (B) reflection of a 20-layer full reflector. (From Ref. 63.)

the UV are several J/cm^2 and S-on-one thresholds are two to four times lower [42].

A recent investigation of 248 nm laser damage of multilayer dielectric stacks employed photothermal displacement and mirage techniques to assess 1-on-1 LIDTs in both fluoride and oxide systems [72]. The study found that LIDT values were dominated by defect absorption within the dielectric layers for a LaF_3/MgF_2 system, and by interface absorption for Al_2O_3/SiO_2 layers. In the case of interface absorption, thermal transport of the energy away from the absorbing region was found to be a critical factor in determining the damage threshold. Mann et al. [74] also found that the substrate's

thermal conductivity was a critical parameter in determining LIDT values of dielectric 248 nm antireflective coatings. The work was extended to 193 nm studies of dielectric-based reflectors. It found significant effects due to hydrocarbon contamination and diffusion into the dielectric layers. Laser conditioning was found to drive out the contaminants and to increase the 193 nm LIDT values.

Few studies have addressed long-term, low-fluence degradation of optical coatings. Two previous studies analyzed UV degradation of dielectric optics at 248 and 308 nm, for exposures up to $\approx 10^8$ pulses and moderately high laser fluences (up to 0.5 J/cm^2/pulse) [74,75]. Both studies reported no visible damage to the coatings, only a slight degradation in optical properties and a possible increase in the absorption coefficient of the dielectric layers.

Within the lifetime of a lithographic tool an average antireflective coating will be subjected to up to 10^{11} pulses at laser repetition rates of 1 kHz and fluences ranging from 0.1 mJ/cm^2/pulse to a few mJ/cm^2/pulse. Since these fluence values are three orders of magnitude below typical single-pulse damage thresholds, one would not expect the coating performance to be determined by LIDT values. Instead, long-term cumulative exposure effects may result either in subtle degradation of optical properties or, perhaps, the eventual failure of the coating. Thus, systematic experiments designed to identify the extent and mechanisms of laser-induced degradation of optical coatings under realistic exposure conditions are needed.

Long-term damage assessment of antireflective coatings for 193 nm lithography was performed at MIT Lincoln Laboratory using incident fluences of <15 mJ/cm^2/pulse and pulse counts of up to 10^9 pulses [50]. Antireflective coatings from nine different commercial suppliers were evaluated under identical conditions. Upon initial irradiation all the coatings underwent a certain amount of surface cleaning, which resulted in higher transmission. The magnitude of this recovery was up to 2%, and its magnitude was found to vary across coatings. This so-called laser cleaning is observed also with bulk materials, but it is more pronounced in coatings, presumably because it is related to surface roughness and/or porosity.

A variety of catastrophic failures of coatings were also observed, although these tended to occur early in the course of the irradiation studies, at pulse counts under 100×10^6. The failure phenomena included high losses, either in the layers or at the interfaces, peeling of the coating, or an apparent thinning of the layers.

It was also noted in these studies that antireflective coatings on fused silica had ~1% higher 193 nm transmission than coatings deposited on calcium fluoride substrates. In the course of 193 nm laser irradiation these losses decreased to the level of the losses on the SiO_2 substrates. This cleaning was very slow, and could take place over 10^9 pulses. No correlation was found between surface roughness and the amount of optical losses. The losses are believed to be an interface phe-nomenon, and the “laser cleaning” perhaps a slow, laser-induced out-diffusion of contaminants through the coating layers.

Thin-film coatings at 157 nm are only now beginning to emerge with the performance and durability comparable to that observed in 193 nm lithography. The main difficulties are qualitatively the same as at longer wavelengths, but quantitatively more pronounced: a limited choice of materials, larger impact of contaminants, as well as the lack of a robust metrology infrastructure.

VII. ATMOSPHERIC ABSORPTION AND SURFACE CONTAMINATION

A critical issue for the operation of optical components and for metrology at short wavelengths is the high absorption coefficient of vapors and surface adsorbates. As can be seen from Figure 11, propagation of UV radiation becomes progressively difficult below 200 nm due to gas-phase absorption by O_2 and H_2O molecules [76]. Even at 193 nm, purging the laser beamline with nitrogen is recommended to suppress ozone formation. By comparison, 157 nm radiation can propagate in an air atmosphere only over distances on the order of a millimeter before being completely absorbed.

Beam delivery systems in the VUV spectral region may be purged with an inert gas or with nitrogen, which is transparent to wavelengths below 120 nm. As an alternative, experiments may be performed under vacuum. However, great

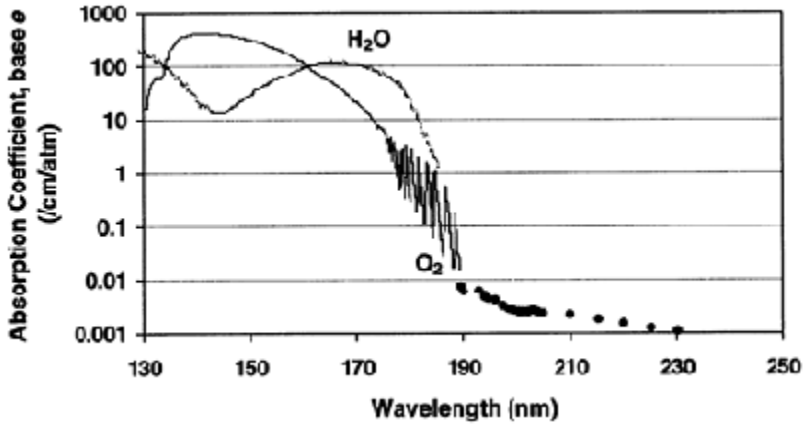

Figure 11 Absorption coefficients of water vapor and oxygen throughout the ultraviolet range. (From Ref. 76.)

care must be taken that the vacuum is established by an oil-free pump and that ultrahigh vacuum techniques are practiced to prevent surface contamination of samples from gas-phase adsorbates. Figure 12 shows that 30 min exposure of a precleaned CaF_2 sample to a 5×10^{-5} torr of vacuum resulted in a transmission drop of several percent throughout the VUV range [24]. In that example, the vacuum was maintained by an oil-free turbomolecular pump backed by an oil-based roughing pump. The contamination can be explained by backstreaming of hydrocarbon-based oils into the vacuum chamber. Note that the original sample transmission could be completely restored by in situ 157 nm laser cleaning.

Ambient contamination and sample packaging can drastically affect measurements in the VUV region. To put the absorptivity of contaminants in perspective, Figure 13 shows the absorption of liquid water and solid polyethylene, a representative material for

modeling common organic contaminants such as alkanes [77]. Even a very thin film of 1 nm organic material can cause a 1% transmission drop at 157 nm. For a 1 nm layer of water, an almost 2% drop in transmission is expected. In fact, in one set of experiments, in the course of sample exchange with a supplier of optical coatings, several antireflectance coatings inadvertently came in contact with a clean polyethylene packaging membrane. All

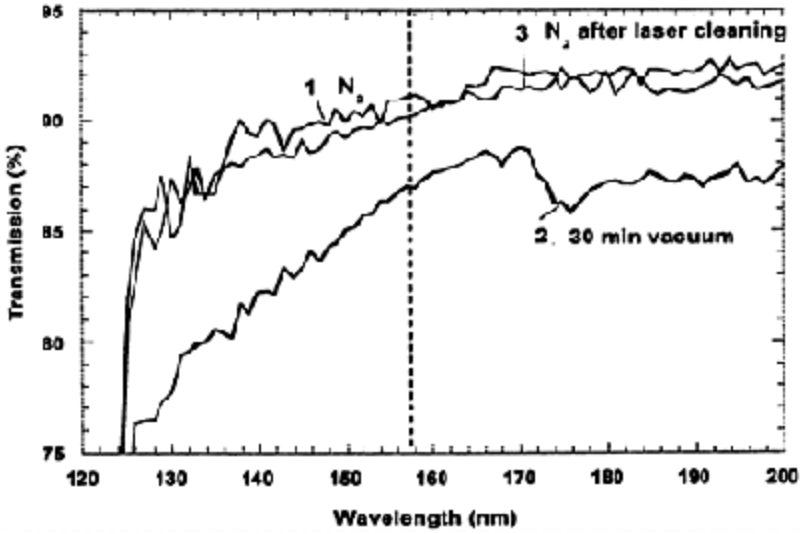

Figure 12 Ambient effects on transmission of a 2 mm thick piece of CaF_2 in the VUV range. (From Ref. 24.)

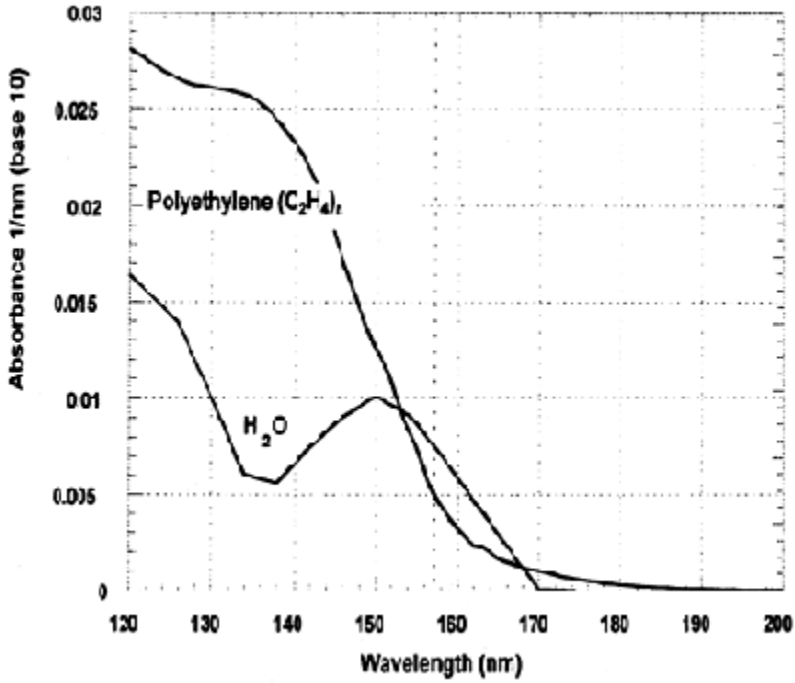

Figure 13 Absorbance per nanometer of a thin layer of polyethylene and condensed water. (From Ref. 77.)

these samples consistently exhibited transmission around 70% when measured in the VUV spectrometer prior to laser exposure. However, upon brief exposure to 157 nm irradiation, dramatic transmission recovery was observed (>25% increase in transmission). By comparison, coating samples shipped in such a way that only an edge contact was made inside the shipping container exhibited only a modest transmission increase (about 1–2%). The effect of surface contamination on samples may be expected to be more dramatic than on uncoated ones because of the possibility of detuning of the dielectric stack and because of the inherent porosity of some dielectric layers, as has been discussed in Sec. VI.

ACKNOWLEDGMENTS

The authors thank all the people and organizations that over the last few years have provided us with samples to be tested and have shared with us their vast amounts of technical insight. Special thanks to our colleagues at MIT Lincoln Laboratory, without whom much of the data reported here would have been impossible to obtain. This work was sponsored in part by the Advanced Lithography Program of the Defense Advanced Research Projects Agency, under Air Force contract F19628–95–C–0002 and in part

under a Collaborative Research and Development Agreement between MIT Lincoln Laboratory and SEMATECH. Opinions, interpretations, conclusions, and recommendations are those of the authors and are not necessarily endorsed by the United States Government.

REFERENCES

1. AI Ershov, T Hofmann, WN Partlo, IV Fomenkov, G Everage, PP Das, D Myers. Proc SPIE 3334:1021–1030, 1998.
2. U Stamm, R Patzel, J Kleinschmidt, K Vogler, W Zschocke, I Bragin, and D Basting. Proc SPIE 3334:1010–1013, 1998.
3. TP Duffey, T Embree, T Ishihara, R Morton, WN Partlo, T Watson, R Sandstrom. Proc SPIE 3334:1014–1020, 1998.
4. R Sandstrom. Proc SPIE 1264:505–519, 1990.
5. K Vogler, U Stamm, I Bragin, F Voss, SV Govorkov, G Hua, J Kleinschmidt, R Paetzel. Proc SPIE 4000:1515–1528, 2000.
6. CB Collins, FW Lee, JM Carrol. Appl Phys Lett 37:857–859, 1980.
7. U Stamm, W Zschocke, B Nikolaus, P Genter, D Basting. Proc SPIE 2991:194–200, 1997.
8. T Uchimura, T Onoda, C-H Lin, T Imasaka. Rev. Sci. Instrum. 70:3254–3258, 1999.
9. Oriel Company. http://www.oriel.com/homepage/down/pdfla.htm
10. Ushio Semiconductor Company http://www.ushiosemi.com/excimer.htm
11. W Tiffany. http://www.molectron.com/AppNote005a.html
12. V Liberman, M Rothschild, JHC Sedlacek, RS Uttaro, AK Bates, K Orvek. Proc SPIE 4000:488–495, 2000.
13. ML Dowell, CL Cromer, RW Leonhardt, TR Scott. AIP Proc 449, 539–541, 1998.
14. JD Buck. http://www.molectron.com/AppNote002a.html
15. Hamamatsu Company. http://usa.hamamatsu.com/opto-semi/photodiodes/default.htm
16. R Gupta, KR Lykke, P-S Shaw, JL Dehmer. Proc SPIE 3818:27–33, 1999.
17. Mc Pherson Inc. http://www.mcphersoninc.com/detectors/model650detectorassembly.htm
18. V Liberman, M Rothschild, JHC Sedlacek, RS Uttaro, A Grenville, AK Bates, C Van Peski Opt Lett 24:58–60, 1999.
19. NV Morozov. Proc SPIE 2428:153–169, 1995.
20. KR Mann, E Eva. Proc SPIE 3334:1055–1061, 1998.
21. R DeSalvo, AA Said, DJ Hagan, EW Van Stryland, M Sheik-Bahae. IEEE J Quantum Electron. 32:1324–33, 1996.
22. E Eva, K Mann. Appl Surf Sci 109–110, 52–57, 1997.
23. R Gupta, JH Burnett, U Griesmann, M Walhout. Appl Opt 37:5964–5968, 1998.
24. TM Bloomstein, V Liberman, M Rothschild, DE Hardy, RB Goodman. Proc SPIE 3676:342–349, 1999.
25. V Liberman, TM Bloomstein, M Rothschild. Proc SPIE 3998:480–491, 2000.
26. JA Woollam, B Johs, CM Herzinger, J Hilfiker, R Synowicki, CL Bungay. Proc SPIE CR72, 3–28, 1999.
27. B Johs, JA Woollam, CM Herzinger, J Hilfiker, R Synowicki, CL Bungay. Proc SPIE CR72, 29–57, 1999.
28. JN Hilfiker, B Sing, RA Synowicki, CL Bungay. Proc SPIE 3998:390–398, 2000.

29. P Boher, JP Piel, P Evrard, C Defranoux, M Espinosa, J Stehle. Proc SPIE 3998: 379–389, 2000.
30. DL Griscom. J Ceram Soc Jpn 99:923–942, 1991.
31. DL Griscom. Proc SPIE 541:38–59, 1985.
32. IT Godmanis, AN Trukhin, K Hubner. Physica Status Solidi B 116:279–287, 1983.
33. S Sakaguchi, S Todoroki, S Shibata. J Am Ceram Soc 79:2821–2824, 1996.
34. DJ Krajnovich, IK Pour, AC Tam, WP Leung, MV Kulkarni. Opt Lett 18:453–455, 1993.
35. DR Sempolinski, TP Seward, C Smith, N Borrelli, C Rosplock. J Non Crystal Solids 203:69–77, 1995.
36. P Schermerhorn. Proc SPIE 1835:70–79, 1992.
37. R Schenker, L Eichner, H Vaidya, S Vaidya, WG Oldham. Proc SPIE 2440:118–25, 1995.
38. S Thomas, B Kuhn. Proc SPIE 2966:56–64, 1996.
39. RE Schenker, WG Oldham. J Appl Phys 82:1065–1071, 1997.
40. C Pfleiderer, N Leclerc, KO Greulich. J Non Crystal Solids 159:145–153, 1993.
41. E Eva, K Mann, S Thomas. Proc SPIE 2966:72–99, 1997.
42. SS Wiseall, DC Emmony. Proc SPIE 369:521–526, 1983.
43. E Eva, K Mann. Appl Phys A 62:143–149, 1996.
44. JH Stahis, MA Kastner. Philos Mag 49:357–362, 1984.
45. V Uhl, KO Greulich, S Thomas. Appl Phys A 65:457–462, 1997.
46. TE Tsai, DL Griscom. Phys Rev Lett 67:2517–20, 1991.
47. C Smith, NF Borrelli, DC Allan, TP Seward. Proc SPIE 3051:116–21, 1997.
48. RJ Araujo, NF Borrelli, C Smith. Proc SPIE 3424:2–9, 1998.
49. V Liberman, M Rothschild, JHC Sedlacek, RS Uttaro, A Grenville, AK Bates, CK Van Peski. Proc SPIE 3427:411–419, 1998.
50. V Liberman, M Rothschild, JH Sedlacek, RS Uttaro, AK Bates, CK Van Peski. Proc SPIE 3578:2–15, 1999.
51. V Liberman, M Rothschild, JHC Sedlacek, RS Uttaro, A Grenville. J Non Cryst Solids 244:159–171, 1999.
52. N Leclerc, C Pfleiderer, H Hitzler, J Wolfrum, KO Greulich, S Thomas, W English. J Non Crystal Solids 149:115–121, 1992.
53. V Liberman, M Rothschild, JHC Sedlacek, RS Uttaro, AK Bates, C Van Peski. Proc SPIE 3679:1137–1142, 1999.
54. TP Duffey, T Embree, T Ishihara, R Morton, WN Partlo, T Watson, R Sandstrom. Proc SPIE 3334:1014–1020, 1998.
55. DC Allan, C Smith, NF Borrelli, TP Seward III. Opt Lett 21:1960–1962, 1996.
56. NF Borrelli, C Smith, DC Allan, TP Seward, III. J Opt Soc Am B 14:1606–15, 1996.
57. RG Morton, RL Sandstrom, GM Blumenstock, Z Bor, CK Van Peski. Proc SPIE 4000:496–510, 2000.
58. CB Norris, EP EerNisse. J Appl Phys 45:3876–3882, 1974.
59. JE Shelby. J Appl Phys 50:3702–3706, 1979.
60. JA Ruller, EJ Friebele. J Non Crystal Solids 136:163–72, 1991.
61. CM Smith, LA Moore. Proc SPIE 3676:834–841, 1999.
62. Y Ikuta, S Kikugawa, T Kawahara, H Mishiro, N Shimodaira, A Masui, S Yoshizawa. Proc SPIE 4000:1510–1514, 2000.
63. V Liberman, TM Bloomstein, M Rothschild, JHC Sedlacek, RS Uttaro, AK Bates, CV Peski, K Orvek. J Vac Sci Technol B 17:3273–3279, 1999.
64. BG Ravi, S Ramasamy. Int J Mod Phys B 6:2809–2836, 1992.

65. DR Rao, HN Bose. J Phys Soc Jpn 28:152–7, 1970.
66. F Abba, Y Marqueton, EA Decamps. Physica Status Solidi A 35:129–132, 1969.
67. JH Burnett, R Gupta, U Griesmann. Proc SPIE 4000:1503–1509, 2000.
68. S Majewski, MK Bentley. Nucl Instrum Methods Phys Res A, Accel 260:373–376, 1987.
69. P Laporte, JL Subtil, M Courbon, M Bon, L Vincent. J Opt Soc Am 73:1062–1069, 1983.
70. S Ogura, N Sugawara, R Hiraga. Thin Solid Films 30:3–10, 1975.
71. U Kaiser, N Kaiser, P Weissbrodt, U Mademann, E Hacker, H Muller. Thin Solid Films 217:7–16, 1992.
72. E Welsch, K Ettrich, H Blaschke, P Thomsen-Schmidt, D Schafer, N Kaiser. Opt Eng 36:504–14, 1997.
73. F Rainer, WH Lowdermilk, D Milam, CK Carniglia, TT Hart, TL Lichtenstein. Appl Opt 24:496–500, 1985.
74. K Mann, B Granitza, E Eva. Proc SPIE 2966:496–504, 1997.
75. DJ Krajnovich, M Kulkarni, W Leung, AC Tam, A Spool, B York. Appl Opt 31: 6062–75, 1992.
76. H Okabe, Photochemistry of Small Molecules. New York: Wiley Interscience, 1978.
77. ED Palik, ed. Handbook of Optical Constants of Solids. vol. 2. San Diego, CA: Academic Press, 1991.

2
Laser Optogalvanic Spectroscopy of Discharge Plasmas in the Ultraviolet Region

C.Haridass,* H.Major, and Prabhakar Misra
Howard University, Washington, D.C.

Xianming L.Han
Butler University, Indianapolis, Indiana

I. INTRODUCTION

The optogalvanic effect (OGE) is due to a change (increase or decrease) in the electrical properties (conductivity) within a self-sustained gaseous discharge when illuminated by radiation that is resonant with an atomic or molecular transition of the element within the discharge. The main principle of this effect is that the absorption of radiation causes a redistribution of populations in the atomic or molecular energy levels. Under steady-state discharge conditions, there exists a dynamic equilibrium (as a result of various radiative and/or collisional and/or collective processes) between the various plasma species causing a well-defined impedance to the flow of current. At dynamic equilibrium, changes in the electron/ion densities and/or mobilities, with a concomitant change in the electrical impedance of the plasma, are caused by optical perturbations. Such a change in impedance alters the current in the plasma and can be either real for direct current (DC) discharges or complex for alternating current (AC) discharges.

The optogalvanic effect has been used for many years as a sensitive and reliable method for recording calibration spectra when tunable lasers are employed for monitoring species (e.g., the hydroxyl radical, OH) that are of primary

* *Current affiliation:* Belfry School, Belfry, Kentucky.

importance to stratospheric photochemistry or tropospheric air quality. Optogalvanic spectroscopic/detection methods are well-established techniques, although the optogalvanic effect in discharges is not completely well understood. Optogalvanic spectroscopy in a gas discharge plasma is differentiated from other charged particle detection techniques, such as space-charge-limited diodes [1] and gas-filled proportional counters [2], by the presence of a sustained discharge involving an electron gas at a relatively high temperature (0.5–10 eV) [3]. Laser optogalvanic (LOG) spectroscopy is performed by directing a tunable dye laser beam into a plasma (such as that generated in a hollow cathode discharge lamp). When the wavelength of the laser beam coincides with the absorption of a species in the plasma, the rate of ionization of that species changes momentarily because of laser-perturbed collisional ionization. The associated impedance

change can be detected as a voltage drop across a ballast resistor in the lamp feeding circuit.

If the laser photon flux is high enough, ionization can occur due to the laser photoionization of excited-state species produced by stepwise resonant or multiphoton laser excitation (whereby the collisional step is replaced by photoionization). The term resonance ionization spectroscopy (RIS) or multiphoton ionization (MPI) is then used. MPI may also be referred to as resonance multiphoton ionization or (REMPI). RIS and MPI differ from the optogalvanic effect in that while they both occur in the plasma/flame environment, they do not necessarily require such a medium [4].

II. OVERVIEW OF PAST AND PRESENT WORK

The earliest observation related to the OGE was made by Foote and Mohler [5]. They used a tungsten lamp dispersed by a monoehromator while studying the photoionization of Cs vapor in a thermionic diode tube, in an effort to detect small levels of ionization. These authors also observed ionization of the Cs occurring when the sample was irradiated by wavelengths longer than 318 nm, which corresponded to wavelengths of the atomic Cs spectrum. They postulated that radiation at these wavelengths produced excited-state atoms, which upon collision with other atoms acquired sufficient additional energy to become ionized. Penning [6] observed the OGE for atoms when he detected a variation in the impedance of a neon discharge irradiated by emission from an adjacent neon discharge. Terenin [7] observed the phenomena in molecules when he studied photoionization of salt vapors. Garscadden et al. [8] observed the OGE brought about by a change in the discharge current of a gas-discharge laser when the laser came over threshold.

It was not until the development of tunable dye lasers, however, that the OGE became widely used as a spectroscopic tool. Green et al. [9] demonstrated that high-sensitivity spectra of the species in a discharge could be obtained with a tunable dye laser. The electronic excitation of the atoms in the discharge allowed for the observation of transitions starting from the metastable or excited states, while the use of a hollow-cathode discharge made it possible to perform spectroscopy on a gas-phase sample of refractory elements produced by cathodic sputtering. Optogalvanic transitions were observed for various species sputtered from hollow cathodes [10–13] and from gas-discharge flashlamps filled with neon and argon [9,14–20]. Optogalvanic signals from commercial neon lamps, extensively used as spectral light sources, have been reported in the 540–750 nm [9,14,16,21] and 2440–2780 nm [15] regions. Gusev and Kompanets [22] pointed out the difficulty of obtaining OG resonances with neon at wavelengths shorter than 580 nm, owing to low oscillator strengths of the resonances. Zhu et al., [23] however, observed laser-assisted OG signals with neon in the 337–598 nm region using a commercial iron-neon hollow cathode lamp. These authors identified 223 OG transitions associated with neon energy levels and found that there were more neon OG lines in the near UV region than in the yellow and red region and that these UV transitions possessed fairly strong intensities. The identified lines in the study by Zhu et al. [23] were calibrated with interference fringes from the two surfaces of an etalon recorded

simultaneously with the OG signal. OG transitions of argon have also been observed in the following wavelength regions: 367–422 nm [20], 415–670 nm [17], 425–700 nm [22], 420–740 nm [18], 555–575 nm [24], 727–772 nm [16], 360–740 nm [19], and 2440–2780 nm [15].

Most of the work cited above, for both neon and argon, describes the general nature of the optogalvanic signals in various wavelength regimens. However, very few studies [25,26,27] reported in the literature identify and quantitatively characterize the dominant physical processes contributing to the production of the optogalvanic signals in a discharge plasma. Han et al., [25] using a simple mathematical rate equation model, with only a few parameters characterizing the atomic state population, produced a good simulation for the observed time-dependent OG waveform for a specific neon transition. In contrast, a model given by Stewart et al. [27] used nearly 150 parameters for the same transition of the neon atom and still failed to describe the observed waveform satisfactorily.

Owing to its sensitivity and selectivity, the optogalvanic technique has been used successfully for a wide variety of laser spectroscopic experiments, including analytical flame spectroscopy/spectrometry [28–30], laser calibration [11,14,19], laser stabilization [31,32], plasma diagnostics [33–34], atomic spectroscopy [4,21], molecular spectroscopy [35–38], and dynamics [39–41].

Turk et al. [28] introduced analytical flame spectrometry using laser-enhanced ionization (the optogalvanic effect in flames). They compared their detection limits to other methods of the time and found competitive sensitivity for a number of elements with a much simpler system. While aspirating a dilute sodium solution into the flame, a measurable increase in the current through the flame was observed when the laser wavelength was tuned to the sodium resonance lines at 589.0 nm and 589.6 nm. The signal responded linearly to Na concentrations in the range 2–1000 ng/ml [29].

Skolnick [31] used the OGE as a method to stabilize the frequency of a single J value CO_2 laser to the center of its output power. Skolnick's method of frequency stabilization was based on modulation of the laser frequency and simultaneous sensing of the resulting perturbation of the laser plasma tube's impedance. Such stabilization resulted in a simple frequency-control system without using a 10 μm light detector or any ancillary optical component [31].

Ausschnitt et al. [33] demonstrated the application of multiphoton optogalvanic spectroscopy to hydrogen discharge plasma diagnostics. The ground and excited-state densities and the translational temperatures of hydrogen and deuterium atoms within the plasmas were probed [33]. The use of two unequal energy photons resonant with an intermediate state enabled three-dimensional probing of the ground state and discrimination between hydrogen and deuterium.

The first LOG detection of molecular ions (N_2^+ and CO^+) was reported by Walkup et al. [38] Their results indicated an optogalvanic mechanism that involves direct alteration of ion mobility by laser excitation due to a difference in charge-exchange collision rates for excited versus ground-state ions. This technique proved to be a sensitive probe of ions in the cathode dark space [38]. The LOG spectroscopic technique may be regarded as a complement to the traditional absorption or fluorescence methods rather than a replacement.

Intermodulated optogalvanic spectroscopy (IMOGS), a newer method of Doppler-free saturation spectroscopy, was described by Lawler et al. [42] Closely related to intermodulated fluorescence spectroscopy, IMOGS, uses the detection scheme of optogalvanic spectroscopy. The authors compared the sensitivity of IMOGS to that of Doppler-free saturated absorption spectroscopy. Using appropriate parameters in their experiment, they estimated that $(S/N)_{IMOGS}/(S/N)_{SAS}= 100$. Since other spectroscopic techniques have been devised that can improve the sensitivity of saturated interference spectroscopy, they concluded that IMOGS would be most useful in the region of the spectrum where low-noise detectors, interferometric-quality optics, or high-quality polarizers were unavailable.

In order to comply with environmentally mandated regulations, the US Department of Energy is attempting to implement online, real-time monitors (with limits of detection of 1 pCi 1^{-1}) to measure the concentration of radionuclides in the off-gases of mixed hazardous waste and radioactive waste thermal treatment systems [43–44]. A detection limit of 1 pCi 1^{-1} corresponds to 465 μg m^{-3} for U-235 and 2980 μg m^{-3} for U-238. Abhilasha et al. [43] developed a LOGS system to measure the concentration of uranium present in the off-gases of mixed hazardous waste thermal treatment systems. Their technique yielded limits several orders of magnitude below that attainable by current real-time online radioactive disintegration counting methods and that sought by US Department of Energy (4.6 μg m^{-3} corresponding to a detection limit of 0.0099 pCi 1^{-1} for U-235 or 0.0016 pCi 1^{-1} for U-238). It was noted, however, that the bandwidth of their current laser system (nominally 0.4 cm^{-1} in the UV) was insufficient to resolve the uranium isotopically.

A field-deployable LOGS system was developed by Monts et al. [44] more recently to measure the concentration of metal species present in thermal treatment systems. LOGS is an ultrasensitive diagnostic tool for online real-time measurements of the concentration of volatile toxic trace metals, radionuclides, and other gas-phase pollutants present in off-gases of mixed-waste thermal treatment systems, where metal species exist primarily as airborne metal oxides and/or metallic particles rather than as free single atoms. Real-time monitoring of airborne contaminants plays a vital role in the protection of personnel and in safe-guarding the environment [44]. Since the amplitude of the LOGS signal can be related to species concentration, LOGS has the capability of monitoring, in real time, the concentration of a pollutant of interest.

Miron et al. [39] studied the dynamics of the OGE in hollow cathode lamps by recording time-dependent OG signals and treating the hollow cathode lamp (HCL) as a circuit element. They found that a stable operation of the HCL does not require a high-impedance source, like that needed for a longitudinal discharge tube (for pressure ranges of 1–10 torr). The investigators reported that the duration of the OG signal (a few microseconds) is independent of the lifetime (10–500 ns) of excited levels populated by the laser. They concluded that it was in fact the impulse response of the electronic circuit (which includes the HCL). The variation of the response time with current implied that the discharge recovered more quickly with increased electron density.

This chapter will fill a gap that exists in the optogalvanic spectral map in the near ultraviolet (UV) region, and study the time-dependent OG waveforms of neon and argon, in order to determine the dominant process or processes affecting the OGE and thereby

quantify important associated rate parameters. Argon and neon are excellent choices for especially accomplishing the first objective, because they are commonly used buffer gases within hollow cathode lamps and provide an acceptable density of lines in the visible and near (UV) regions. The near UV region is of importance because in this wavelength domain fall the electronic spectra of important atmospheric and combustion species, which include chemical intermediates such as the hydroxyl and alkoxy radicals. The second and more ambitious objective was complicated because the environment of a discharge is too complex to be described by a single general theoretical model; and a quantitative understanding of the OGE is possible only if a reasonable model of the discharge can be made and the cross sections of the involved processes are well known. An effective use of the rate equation formalism to describe the different discharge processes can lead to a very large number of equations for which cross-section values are unavailable. Thus, any knowledge of the prop-erties of a particular discharge is usually largely empirical. An extended and refined version of a mathematical rate equation model for the population distribution of the atomic species in a commercial hollow cathode discharge lamp, set forth by Han et al. [25] in a relatively recent paper on collisional ionization in a discharge plasma, was used in this investigation. The time-resolved profiles of LOG waveforms of argon and neon were analyzed using commercial hollow cathode discharge lamps, with an emphasis on the low-discharge current regimen (0.2–3.0 mA), since it had not been covered in previous studies and promised to provide new insight into multilevel atomic systems in a gas discharge plasma. The physics of time-resolved OG waveforms provided quantitative information on the rates of excited-state collisional processes in a gas discharge plasma.

Collisional ionization is a primary chemical process occurring in the upper atmospheres and in ionospheres of planets. The flux of energetic photons in the upper atmosphere can induce chemical reactions that are extremely difficult to reproduce under similar conditions in the laboratory. An understanding of the ionization processes and the subsequent chemistry is essential for answering questions such as the phenomenon responsible for the existence of sharp ionization layers (so-called ledges), or to the ionic contributions of various physical phenomena, such as thermospheric heating and auroral excitations. The study of the optogalvanic effect may provide some critical insights into more effective parameterization in models of ionospheric excitation. Neon and argon are good candidates for prototype studies because they do not posses rotational or vibrational degrees of freedom. However, neon is isoelectronic with HF, CH_4, and other trace gases, while argon is isoelectronic with HCl, F_2, and other species. By studying the collisional excitation of these noble gases under controlled conditions, suitable approximations can be made to explain the behavior of important trace gases in the upper atmosphere. By fitting the OG waveforms, parameters associated with rates of decay and those proportional to the cross sections of electron collisional ionization are obtained. Allowances have to be made for rotational and vibrational degrees of freedom, and decay rates obtained would probably not be very accurate, but there should be many similarities between the neon/ argon prototype and a so-called unified atom framework of the trace gases.

III. EXPERIMENTAL WORK

The experimental arrangement used for laser optogalvanic spectroscopy is shown in Figure 1. In this figure, a dye laser (DL) is pumped by the second harmonic of a Nd:YAG-laser (YL) running at 10 Hz. The output beam had a pulse duration of about 20 ns and a nominal line width of 0.07 cm^{-1} (without any intracavity etalon). The tuning range in the near UV (and visible) was covered by several laser dyes. One of the beams passed through a 1 mm aperture and entered either

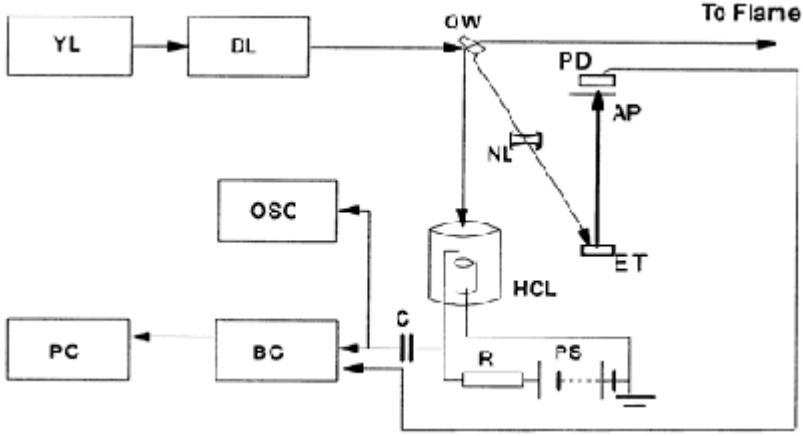

Figure 1 Schematic experimental arrangement for laser optogalvanic spectroscopy YL, Nd:YAG laser; DL, dye laser; QW, quartz wedge; PD, photodiode; AP, aperture; NL, negative lens; ET, etalon; HCL, hollow cathode discharge lamp; PS, power supply; R, resistor; C, capacitance; BC, boxcar; OSC, oscilloscope; PC, personal computer.

a commercial (Perkin-Elmer) iron-neon HCL or a Laser Galvatron (L2783–26ANE-FE, Hamamastu Co.), which is also an HCL containing argon (2 Torr), neon (3 Torr), and trace amounts of iron vapor. The second split beam can be directed to record simultaneously the laser-induced fluorescence (LIF) spectrum of a free radical (e.g., OH) in a propane-air flame. An interference fringe pattern was also simultaneously recorded using the etalon for calibration purposes. A high-voltage power supply (PS) and a ballast resistor (R) of 20 KΩ for the ironneon lamp (and 30KΩ for the Ar-containing commercial Laser Galvatron) were used to record the OG spectra. When the laser pulse was resonantly absorbed by the discharge medium, the voltage across the lamp varied, and these variations were suitably coupled via a capacitor (C) to a boxcar (BC) integrator. Temporal evolution of the signal was recorded using a digital oscilloscope (OSC). Outputs of the boxcar and the photodiode were recorded with a computer-aided (PC) data acquisition system.

IV. THEORY

A. Mechanism

The mechanism of the optogalvanic effect involves laser enhancement or suppression of the ionization rates of a particular species present in the plasma. Several models have been developed, each appropriate for a given type of plasma, but they are essentially phenomenological and do not account for many of the complex processes occurring in ionized gases that could, in principle, be involved in a laser-induced impedance change. Yet the fact that a number of different plasma sources exhibit the OGE (flames, positive column DC discharges, hollow cathode DC discharges, radiofrequency (RF) discharges) attests to its generality [37].

Illumination of a gas discharge with radiation at a wavelength corresponding to an atomic transition of a species in the discharge causes perturbations to the steady-state population of two or more levels. This, in turn, causes a change in the electrical properties of the discharge. The optogalvanic effect can correspond to an increase or decrease in discharge current depending on the kinetics of the levels whose populations are perturbed by the laser. When the laser frequency is tuned to the transitions $E_{L1} \rightarrow E_{L2}$ between two levels of atoms or ions in the discharge, the laser initially transfers some population in E_{L1} to E_{L2}, which subsequently relaxes to E_{L3} by radiative and/or collision processes in a tim e frame of tens of nanoseconds. Owing to the different ionization probabilities from E_{L1} and E_{L3}, such a population change will result in a change in the discharge current, ΔI, which is then detected as a voltage change $\Delta V = R\ \Delta I$ across the ballast reqsistor R. In general, positive and negative signals are observed, depending on the characteristics of levels E_{L1} and E_{L3} involved in the transition $E_{L1} \rightarrow E_{L3}$. If IP_{L1} is the total ionization probability of an atom in level E_{L1}, the voltage change ΔV produced by the laser-induced change $\Delta n_{L1} = n^{f}_{L1} - n^{i}_{L1}$ is given by: [45]

$$\Delta V = R\ \Delta I = a[\Delta n_{L1} IP_{L1} + \Delta n_{L3}\ IP_{L3}] \tag{1}$$

where Δn_{L1} is the laser-induced change in the population of level 1 (final—initial) and Δn_{L3} is the change in the population of level 3. If the laser excites atoms from a level E_{L1}, with a small probability of ionization, to a level E_{L3}, which has a larger probability of ionization, the discharge current will increase. If on the other hand, the net effect of the laser takes atoms from a level with a large probability of ionization to a level with a small probability of ionization, the discharge current will decrease. The latter often arises when the atom is excited out of a long-lived metastable state into a higher-lying state that is not metastable, which results in rapid decay to a state lower than the original metastable state. Some of the lowest excited levels in noble gases are metastable, having values of $J=0$ or 2. Metastable atoms exist in high concentrations in glow discharges and thus can have a great impact on the optogalvanic effect.

The convention used throughout the present study is based on an external measuring circuit that takes the OG signal off the cathode end of the discharge lamp. The traditional

positive OG signal is one in which there is a net increase in ionization or increase in current ($\Delta I>0$). It is the result of a decrease in impedance, which appears as a decrease in voltage ΔV across the HCL (or an increase in voltage across the ballast resistor) that causes the waveform to appear with an initial negative peak. A *negative* OG signal results from the depletion of the metastable population. The net effect is an increase in impedance and therefore an increase in ΔV, whereby $\Delta I<0$. (Note: When signals are measured from the anode, all signs are reversed.)

Several different ionization reactions can contribute to the discharge current. Electron impact ionization, collisions among the discharge species, and Penning ionization are perhaps the most important and likely candidates. We use the notation: B=buffer gas atom, S=sputtered atom and B*=an excited state of B, so that various ionization processes may be represented as follows.

Electron impact ionization occurs from excited levels as well as from the ground state, and although it is not always the dominant ionizing reaction, it usually contributes to the effect to some degree. It may result from a one-step ionization defined as

$$B+e^- \rightarrow B^+ + 2\ e^- \qquad (2)$$

Such direct ionization dominates at low pressures, since the electrons can acquire enough energy between collisions to ionize an atom. A two-step, or multistep ionization, is also possible and defined by

$$B+e^- \rightarrow B^* + e^-$$
$$B^*+e^- \rightarrow B^+ + 2\ e^- \qquad (3)$$

This kind of process is important in noble gas discharges and has a significant impact on the optogalvanic effect.

Collisions among the excited atoms of the discharge species can be represented by

$$B^*+B^* \rightarrow B^+B+e^- \qquad (4)$$

These types of collisions are mostly seen in the case of noble gas atoms and are very effective because of the high energies (on the order of 16.6 eV for neon and 11.6 eV for argon) of the metastable levels involved. The buffer gas ions liberate atoms from the surface of the cathode by colliding with the cathode material. Thus, the liberated atoms form a minor constituent of the discharge species.

Penning ionization can be represented by

$$B^*+S \rightarrow S^+ + B + e^- \qquad (5)$$

In Penning ionization, the excited buffer gas atoms may ionize the sputtered atoms. This kind of process is important for discharges in noble gases and influences the

characteristics of the observed discharge current. In general, at higher discharge currents, the mechanism of electron impact ionization dominates over Penning ionization, leaving the latter hardly noticeable [46,47].

Broglia et al. [48] demonstrated that photoionization can influence the discharge current in hollow cathode DC lamps. The researchers showed that the dark space of hollow-cathode discharges exhibits signals much more rapidly than the conventional OG signals and related them to direct laser photoionization. Since our work was based on results in which the laser beam is collimated to fill the region between the electrodes, it was first assumed that we might be able to see this feature; however, the energy flux was so weak in the low-current region used in this study that we could not do so. Broglia et al. [49] also admitted that experimental evidence showed that in a low-power regimen only the OG signal characterized by the μs time scale arises.

It was still evident, however, that the induced current resulting from the OGE could, in principle, be due to many factors. One of the main objectives of the present work was to study extensive sets of OG transitions of neon and argon. As expected, the largest identifiable contribution of the OGE waveform turned out to be the electron collisional ionization of the buffer gas, and contributions such as Penning ionization and others only appeared as either slight additions or perturbations.

A nonlinear least-squares fitting program written by Han [50] of Butler University in Fortran code was used and was capable of fitting multiple exponential functions to experimental data of the form:

$$W=ae^{-bt}+ce^{-dt}+ee^{-ft}+\ldots$$

The fit could run up to 200 iterations or until a precision of 10^{-6} was reached. W is the waveform intensity; *a, c, e,*…, etc., are coefficients related to effective collisional cross sections; and *b, d, f,*…, etc., are exponential parameters that allow quantification of the decay rates and thus the effective lifetime of the states involved in the OG transition.

B. Theoretical Model

A model involving only buffer gas (neon or argon) transitions, developed by Han et al., [25] was modified and used in this study to account for the results associated with time-resolved waveforms of LOG transitions. Neon or argon atoms are detected by the optogalvanic effect (via increased or decreased discharge current) only as they are ionized. When the laser is tuned to a transition of the buffer gas, the number of atoms in each state is determined mainly by three processes electron collisional excitation, radiative depopulation, and electron collisional ionization. Certain other nonnegligible processes can contribute to the OG effect: in particular, the redistribution of excited buffer gas atoms due to atomic and electronic collisions. Subsequent relaxation of these atoms to the corresponding lower states may be subject to further ionization. In terms of the Paschen notation, for